Cancer Cell

Article

Neutralizing IL-8 potentiates immune checkpoint blockade efficacy for glioma

Graphical abstract

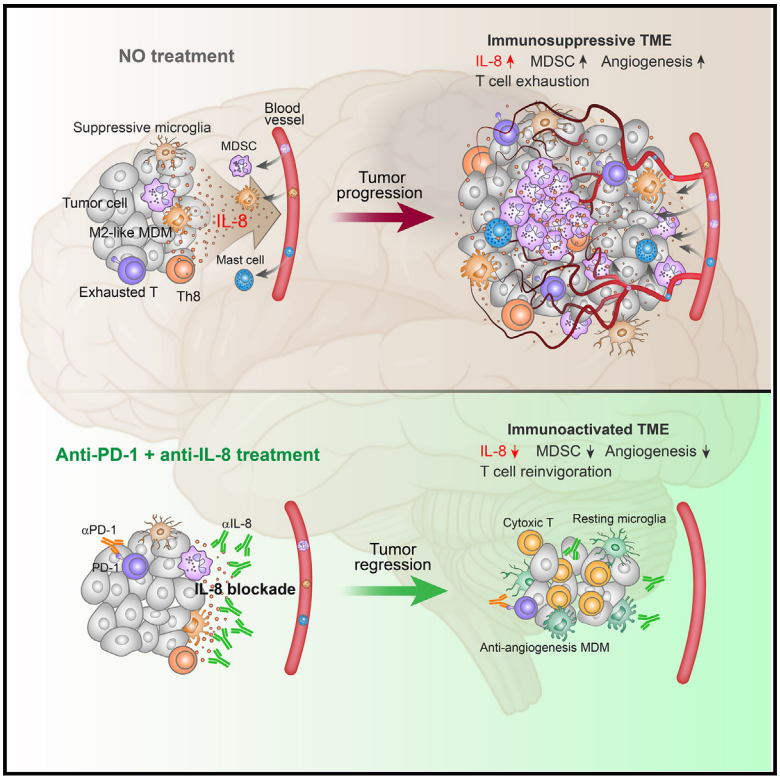

Highlights

- With CCR5 and CXCR3 expression, T cells reside mainly at perivascular cuffs in TME
- Glioma-killing T cells include pre-/exhausted, effector $CD8^+$ T, and cytotoxic $CD4^+$ T subsets
- IL-8^+CD4^+ T (Th8) lineage exhibits innate-like feature and orchestrates TIME
- Inhibition of the IL-8-CXCR1/CXCR2 axis reprograms TME and leverages ICB efficacy

Authors

Haofei Liu, Qiwen Zhao, Leyong Tan, ..., Sheng-Qing Lv, Xiu-Wu Bian, Xindong Liu

Correspondence

wang_yan1977@hotmail.com (Y.W.), lvsq0518@hotmail.com (S.-Q.L.), bianxiuwu@263.net (X.-W.B.), xindongliu@hotmail.com (X.L.)

In brief

Massive MDSC infiltration, pro-tumor TAM polarization, and angiogenesis in glioma constitute barriers to counteract ICB-elicited antitumor immunity. Liu et al. show that IL-8, derived from tumor, myeloid, and T cells, plays a pivotal role in orchestrating TIME in glioma, and blockade of the IL-8-CXCR1/CXCR2 axis unleashes anti-PD-1 efficacy in IL-8-humanized mice.

Liu et al., 2023, Cancer Cell *41*, 693–710
April 10, 2023
https://doi.org/10.1016/j.ccell.2023.03.004

CellPress

Cancer Cell

CellPress
OPEN ACCESS

Article

Neutralizing IL-8 potentiates immune checkpoint blockade efficacy for glioma

Haofei Liu,[1,9] Qiwen Zhao,[1] Leyong Tan,[1] Xin Wu,[1] Rui Huang,[1] Yonglin Zuo,[1] Longjuan Chen,[1] Jigui Yang,[1] Zuo-Xin Zhang,[2] Wenchen Ruan,[1,3] Jiayang Wu,[1,3] Fei He,[4] Yiliang Fang,[1] Fangyuan Mao,[1] Peipei Zhang,[1] Xiaoning Zhang,[1] Peidi Yin,[1] Zexuan Yan,[1] Wenwen Xu,[1] Huimin Lu,[1] Qingrui Li,[1] Mei Liang,[1] Yanjun Jia,[5] Cong Chen,[1] Senlin Xu,[1] Yu Shi,[1] Yi-Fang Ping,[1] Guang-Jie Duan,[1] Xiao-Hong Yao,[1] Zhijian Han,[6] Tao Pang,[3] Youhong Cui,[1] Xia Zhang,[1] Bo Zhu,[7] Chunjian Qi,[8] Yan Wang,[1,*] Sheng-Qing Lv,[2,*] Xiu-Wu Bian,[1,*] and Xindong Liu[1,9,10,*]

[1]Institute of Pathology and Southwest Cancer Center, Southwest Hospital, Third Military Medical University, Chongqing 400038, P.R. China
[2]Department of Neurosurgery, Xinqiao Hospital, Third Military Medical University, Chongqing 400037, P.R. China
[3]Jiangsu Key Laboratory of Drug Screening, State Key Laboratory of Natural Medicines, China Pharmaceutical University, Nanjing 210009, P.R. China
[4]Genergy Biotechnology (Shanghai) Co., Ltd, Shanghai 200235, P.R. China
[5]Chongqing International Institute for Immunology, Chongqing 401338, P.R. China
[6]The Key Laboratory of the Digestive System Tumors of Gansu Province, Department of Tumor Center, Lanzhou University Second Hospital, Lanzhou 730030, P.R. China
[7]Institute of Cancer, Xinqiao Hospital, Third Military Medical University, Chongqing 400037, P.R. China
[8]Medical Research Center, The Affiliated Changzhou No. 2 People's Hospital, Nanjing Medical University, Changzhou 213003, P.R. China
[9]Jinfeng Laboratory, Chongqing 401329, P.R. China
[10]Lead contact
*Correspondence: wang_yan1977@hotmail.com (Y.W.), lvsq0518@hotmail.com (S.-Q.L.), bianxiuwu@263.net (X.-W.B.), xindongliu@hotmail.com (X.L.)
https://doi.org/10.1016/j.ccell.2023.03.004

SUMMARY

Malignant gliomas are largely refractory to immune checkpoint blockade (ICB) therapy. To explore the underlying immune regulators, we examine the microenvironment in glioma and find that tumor-infiltrating T cells are mainly confined to the perivascular cuffs and express high levels of CCR5, CXCR3, and programmed cell death protein 1 (PD-1). Combined analysis of T cell clustering with T cell receptor (TCR) clone expansion shows that potential tumor-killing T cells are mainly categorized into pre-exhausted/exhausted and effector $CD8^+$ T subsets, as well as cytotoxic $CD4^+$ T subsets. Notably, a distinct subpopulation of $CD4^+$ T cells exhibits innate-like features with preferential interleukin-8 (IL-8) expression. With IL-8-humanized mouse strain, we demonstrate that IL-8-producing $CD4^+$ T, myeloid, and tumor cells orchestrate myeloid-derived suppressor cell infiltration and angiogenesis, which results in enhanced tumor growth but reduced ICB efficacy. Antibody-mediated IL-8 blockade or the inhibition of its receptor, CXCR1/2, unleashes anti-PD-1-mediated antitumor immunity. Our findings thus highlight IL-8 as a combinational immunotherapy target for glioma.

INTRODUCTION

Malignant glioma has a very poor prognosis and remains challenging because of the limited options of standard treatment.[1] Although immune checkpoint blockade (ICB) therapy has shown remarkable success in treating a variety of tumors, the clinical benefit of ICB therapies for malignant glioma remains compromised.[2] Potential reasons for this include the intrinsic properties of glioma cells, such as their vast genetic heterogeneity but low mutation burdens, and alternatively the extrinsic feature of a highly immunosuppressive microenvironment governed by prevalent tumor-associated myeloid cells, as well as microvascular niches that sabotage T cell-mediated antitumor immunity.[3–5]

Accumulating evidence indicates that the heterogeneity and functional status of tumor-infiltrating T cells play pivotal roles in shaping antitumor immunity and the response to immunotherapy.[6,7] The glioma microenvironment harbors both $CD4^+$ and $CD8^+$ T cells, although less frequently than myeloid cells;[8–10] they increase paradoxically with tumor grade,[11–14] implying their functional diversity. Indeed, recent efforts focusing on T cell exhaustion assessment at the single-cell level have revealed that glioma-infiltrating T cells comprise variable subpopulations, among which a fraction of T cells are clonally expanded and categorized mainly into exhausted, effector, or memory subsets,[8,15] whereas the remaining large proportion of tumor-infiltrating T cells are not clonally expanded and their function remains unexplored. Here, we conducted landscape mapping of T cells from paired human blood and tumor tissues with adaptations of single-cell RNA sequencing (scRNA-seq), cytometry by time of flight (CyTOF), and flow cytometry. Comparison

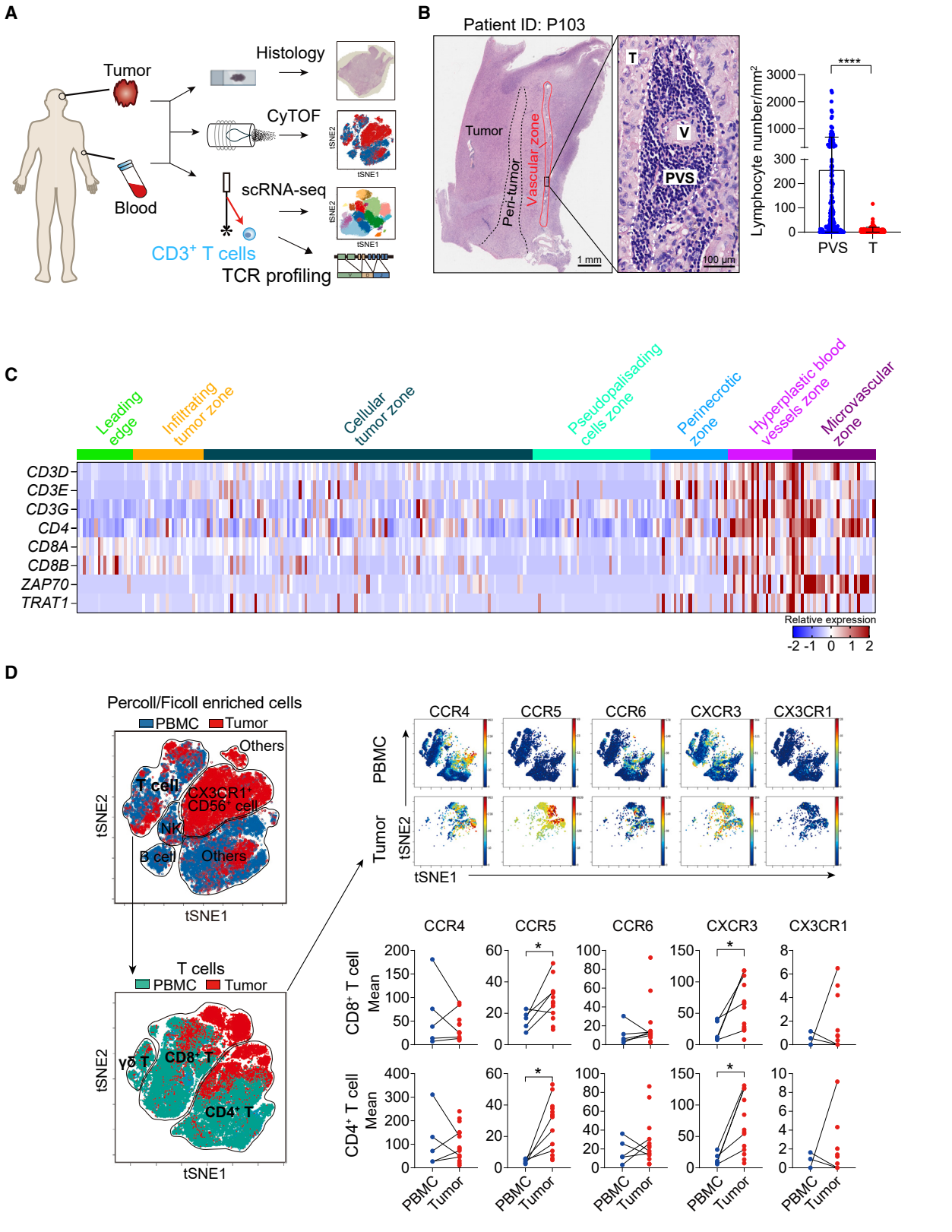

(legend on next page)

analysis enabled us to uncover the unique features of tumor-infiltrating T cells compared with their peripheral counterparts. Specifically, we identified a distinctive subset of interleukin-8 (IL-8)-producing $CD4^+$ T cells that exhibits innate-like features and correlates with poor prognosis. Given that IL-8 is absent in rodents, thus preventing the incisive investigation of IL-8-mediated immune responses *in vivo* and its role in blunting ICB therapy,[16–18] we developed an IL-8-humanized mouse strain by adapting a strategy shown previously.[19] Using this mouse model, we find IL-8^+CD4^+ T cells can function alone and/or together with other IL-8-producing cells to solidify the immunosuppressive properties of the glioma microenvironment. Strikingly, anti-PD-1 immunotherapy elevates systemic IL-8 expression and blunts ICB efficacy by reinforcing immunosuppression. Thus, our study leverages the understanding of bystander T cells in tumors and highlights the IL-8-CXCR1/CXCR2 axis as a combinational immunotherapy target.

RESULTS

Anatomic analysis of tumor-infiltrating T cells in glioma patients

A detailed investigation of functional and transcriptional alterations that occur in T cells between peripheral blood and glioma tissue is needed. To fill this gap, we combined anatomic assessment with high-dimensionality mass cytometry and scRNA-seq to measure T cell residence pattern and transcriptome in tumors, trafficking surface markers and transcriptomics on glioma tissues and peripheral blood samples from 152 human patients: 51 patients with low-grade glioma (LGG) and 101 patients with high-grade glioma (HGG) (Figure 1A). Clinical information for these patients was summarized in Tables S1 and S2.

We first stained tumor tissues from 71 glioma patients, including HGG and LGG, with hematoxylin and eosin (H&E) and immunohistochemistry (IHC). Notably, the majority of the T cells resided at the perivascular cuffs of microvascular zones (Figures 1B and S1A), which was confirmed by anatomic transcriptional atlas data (Ivy Glioblastoma Atlas Project [GAP]) (Figure 1C). To decipher which chemokine receptor navigates T cell infiltration into the glioma, we utilized CyTOF to examine peripheral blood mononuclear cells (PBMCs) and glioma tissue samples from 14 newly diagnosed patients, from whom five paired PBMCs and tissue samples were included. Our results showed that among the tested chemokine receptors, including CCR4, CCR5, CCR6, CXCR3, and CX3CR1, only CCR5 and CXCR3 expressions were significantly elevated on both $CD4^+$ and $CD8^+$ T cells in the tumor compared with peripheral blood (Figure 1D), suggesting that CCR5 and CXCR3 are required to guide T cell migration into glioma. Both $CD4^+$ and $CD8^+$ T cells in the tumors prevalently expressed the exhaustion marker PD-1, but not lymphocyte-activation gene 3 (LAG-3) (Figures S1B and S1C). Also, $CD4^+$ T cell compartment in the tumors enhanced surface CD25 expression as compared with the peripheral counterpart (Figures S1B and S1C), seemingly representing the elevated Treg cell infiltration in glioma.

Single-cell clustering of T cells in glioma

To globally dissect the heterogeneity of the T cell compartment in the tumor microenvironment (TME), we sorted T cells from five freshly dissociated tumors and paired PBMCs and profiled them by scRNA-seq and single-cell T cell receptor (TCR) sequencing (scTCR-seq) with 10× Genomics. We obtained a total of 116,205 T cells (65,990 from PBMCs and 50,215 from tumors) after stringent quality-control filtering. TCR repertoire sequencing identified 67,665 T cells with paired α and β chains. After exclusion of non-tumor-specific TCRs by utilizing the Immune Epitope Database and Analysis Resource (IEDB) tool (Table S3),[20] the remaining potential tumor-reactive TCR clonotype was defined as those paired α and β chains shared by at least two T cells. T cell clusters were classified by their residence, TCR clonality, and signature genes according to previous reports.[7,15,21,22] A total of 18 T cell clusters across both tumor and PBMC samples were identified, including 7 clusters for $CD4^+$ T cells, 10 clusters for $CD8^+$ T cells, and 1 cluster for $\gamma\delta$ T cells, each with unique signature genes (Figures S2A–S2C and 2A). The overall representation of these clusters was similar across five glioma patients (Figure S2B). Specifically, the $CD4^+$ T cell compartment was diversified with seven clusters. The naive subset (C1_CD4_Naive) was predominant in blood (Figures 2B and S2C). The central memory subset (C2_CD4_Tcm) was prevalent in blood and characterized by high expression of the *IL7R*, *TCF7*, *SELL*, and *MYC* genes (Figures 2B and S2C). Clonally expanded cytotoxic subset (C6_CD4_Cyto) cells highly expressed the cytotoxicity-related genes *NKG7*, *GZMA* and *GZMK* (Figures 2B–2D and S2C–S2E; Table S4). A dysfunctional subset (C7_CD4_Dysfun) was also clonally expanded and marked by high expression of the gene encoding inhibitory CTLA-4 and minimal levels of cytotoxicity-related genes (Figures 2C, 2D, and S2C–S2E). Notably, an IL-8-producing subset (C8_CD4_*IL8*) was exclusively enriched in tumors and characterized by high expression of *IL8*, *NINJ1*, *HLA-DRA*, and *HAVCR2* (Figures 2B and S2C). Another nonclonally expanded T cell subset (C9_CD4_Tn-like) highly expressed naive marker genes plus *SOCS3* (Figures 2B and S2C–S2E), thus representing the previously reported naive-like T cell subset.[7] *FOXP3*-expressing regulatory T cell subset (C12_Treg) was clonally expanded, indicative of TCR-dependent activation or differentiation (Figures 2C, 2D, and S2C).

Figure 1. Landscape mapping and anatomic analysis of T cells in glioma

(A) Workflow for sample processing and scRNA-seq, CyTOF, and tissue histology analysis.

(B) Representative examples of hematoxylin and eosin (H&E) staining of glioma tissue among 71 patients. Graph data are displayed as the mean ± standard deviation (SD). n = 186, two to three views from each patient; $^{**}p < 0.01$, two-tailed unpaired t test.

(C) Heatmap of T cell signature gene relative expression in different anatomic locations of glioma. Data were downloaded from the Ivy Glioblastoma Atlas Project (GAP), containing 270 samples from 41 patients.

(D) Left, tSNE plots of Percoll-enriched immune cells and T cells from mass cytometry data are shown. Right, tSNE plots are overlaid with chemokine receptors. PBMC, n = 5; tumor, n = 14. $^{*}p < 0.05$, two-tailed paired t test.

PVS, perivascular space; T, tumor; V, vessel. See also Figure S1 and Tables S1 and S2.

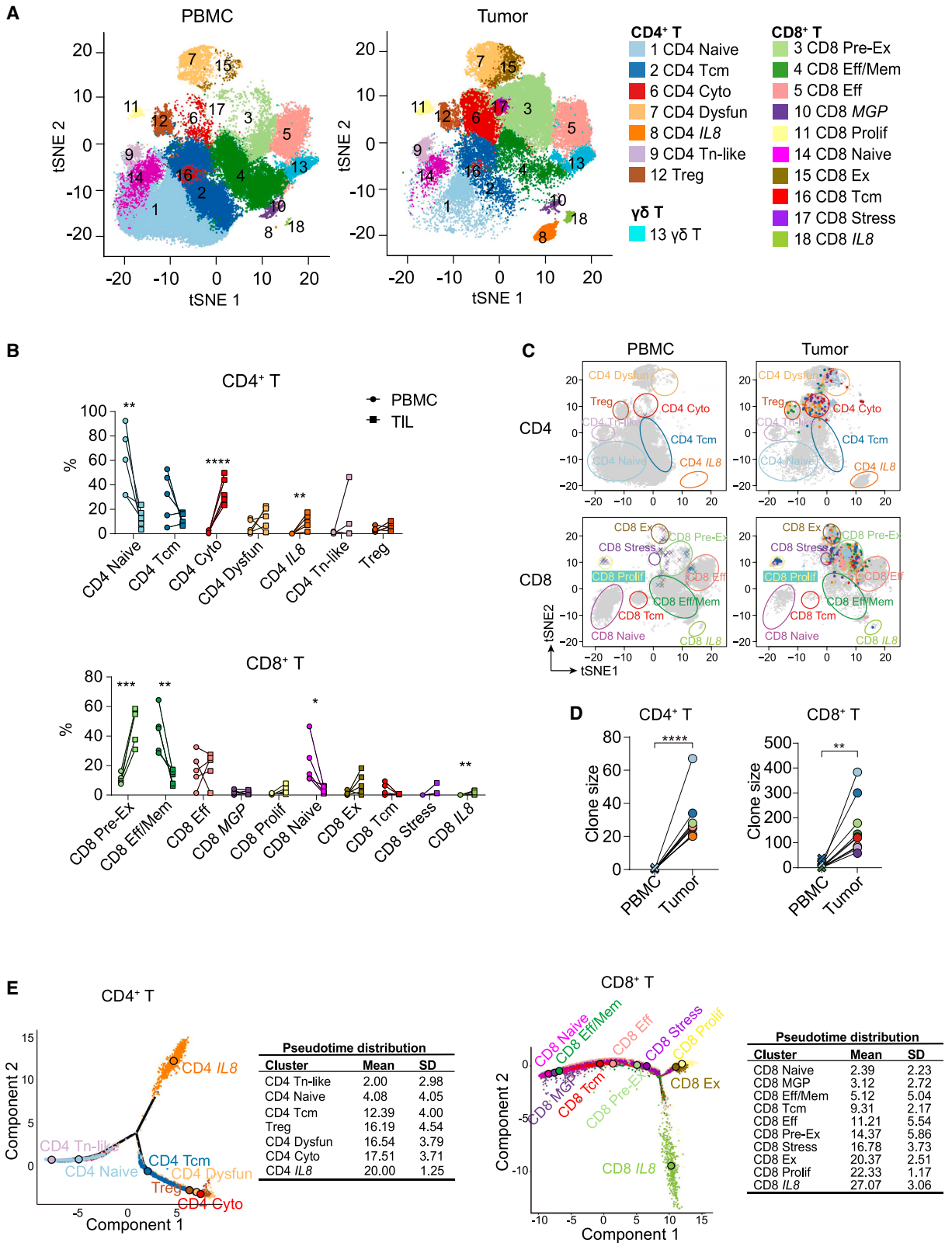

Pseudotime distribution

Cluster	Mean	SD
CD4 Tn-like	2.00	2.98
CD4 Naive	4.08	4.05
CD4 Tcm	12.39	4.00
Treg	16.19	4.54
CD4 Dysfun	16.54	3.79
CD4 Cyto	17.51	3.71
CD4 *IL8*	20.00	1.25

Pseudotime distribution

Cluster	Mean	SD
CD8 Naive	2.39	2.23
CD8 MGP	3.12	2.72
CD8 Eff/Mem	5.12	5.04
CD8 Tcm	9.31	2.17
CD8 Eff	11.21	5.54
CD8 Pre-Ex	14.37	5.86
CD8 Stress	16.78	3.73
CD8 Ex	20.37	2.51
CD8 Prolif	22.33	1.17
CD8 *IL8*	27.07	3.06

Figure 2. Single-cell clustering of T cells

(A) t-distributed stochastic neighbor embedding (tSNE) plots of T cells from PBMCs and tumor tissues.

(B) The percentages of cells in different clusters in PBMCs and tumor tissues.

(legend continued on next page)

Similarly, combinational analysis of the transcriptional signature and TCR clone expansion revealed 10 major clusters for $CD8^+$ T cells (Figures 2A and S2C), and highly clonally expanded T cells (TCR clone size over 10, TCS > 10) were mainly located in the TME (Figures 2B–2D, S2D, and S2E). Clonal $CD8^+$ T cell-enriched subsets included six clusters (Figures S2D and S2E). Pre-exhaustion $CD8^+$ T cells (C3_CD8_Pre-Ex, TCS > 10, 37.8%) expressing effector genes *NKG7*, *GZMA*, *GZMH*, and *GZMK* and surface marker genes *LAG3*, *KLRB1*, *TIGIT*, and *PDCD1*, mirroring the previous identification,[15] were preferentially located at tumor sites (Figures 2B and S2C–S2E). Exhaustion cluster (C15_CD8_Ex, TCS > 10, 17.6%) was marked with exhaustion genes *TOX*, *CTLA4*, *TIGIT*, and *NR4A2* (Figures S2C–S2E). Proliferating subset (C11_CD8_Prolif, TCS > 10, 11.2%) was signatured with the cycling gene *MKI67* (Figures S2C–S2E). Also, effector cluster (C5_CD8_Eff, effector genes *FGFBP2*, *PFR1*, *GZMB*, and *GNLY*) and stress cluster (C17_CD8_Stress, stress signature genes *HSP90AA1*, *HSPA6*, and *HSPA1B*) contained highly clonally expanded T cells (TCS > 10) with a percentage of 10.6% and 8.4%, respectively (Figures S2C–S2E). Notably, effector/memory $CD8^+$ T cells (C4_CD8_Eff/Mem, TCS > 10, 3.6%; effector genes *NKG7*, *GZMA*, and *GZMK*; and memory marker gene *IL7R*) were preferentially enriched in PBMCs (Figures 2B and S2C–S2E). The remaining four nonclonally or low-clonally expanded $CD8^+$ T cell clusters included the naive T cell cluster (C14_CD8_Naive), the central memory subset (C16_CD8_Tcm), the IL-8-producing subpopulation (C18_CD8_*IL-8*), and the *MGP* gene-signatured unknown cluster (C10_CD8_MGP).[23]

To explore the developmental state and ontogenetic relationship of these six highly clonally expanded $CD8^+$ T cell clusters, we conducted pseudotime trajectory analysis along with TCR clonotype assessment. We found that these six different clusters formed developmental orders in the context of the total population of $CD8^+$ T cells, and the effector/memory $CD8^+$ T cluster stayed at the earlier period of the pseudotime, followed sequentially by the effector, pre-exhaustion, stress, proliferation, and exhaustion clusters (Figure 2E). This developmental transition was also independently validated by clonal analysis based on TCR clonotype sharedness. Strikingly, the three most prevalent tumor-enriched $CD8^+$ T cell subpopulations, pre-exhaustion, exhaustion, and effector subpopulations, comprised the majority of the clonal T cells and shared their clones extensively (Figures 2C and S2D–S2F), indicating that they may serve as the main local players in killing glioma tumor cells and remain as the major immunotherapeutic targets for glioma.

In the $CD4^+$ T cell compartment, highly expanded TCR clones appeared mainly at cytotoxicity, dysfunction, and Treg clusters (Figures 2C, S2D, and S2E). Both cytotoxic and dysfunctional $CD4^+$ T cells shared their TCR clones substantially, but these cells barely shared their TCR clones with Treg cells (Figure S2F), which is consistent with the observations from other solid tumors, such as liver cancer.[21] Importantly, regardless of the TCR clone overlaps in the overall T cell population, there were few identical TCR clones when comparing five individual patients (data not shown).

To further specify the differences in T cell transcriptional status at tumor sites between LGG and HGG, we expanded scRNA-seq sample sizes to 13 (4 from LGG patients and 9 from HGG patients). Comparative analysis revealed that the overall representation of T cell clusters was similar between LGG and HGG (Figures S2G and S2H), and only the frequency of the naive-$CD4^+$ T subset (C1_CD4_Naive) was significantly higher at tumor sites in LGG than that in HGG (Figure S2H). In contrast, HGG tumor tissues exhibited a pattern of higher frequencies of IL-8-expressing $CD4^+$ T subset (C8_CD4_*IL8*, $p = 0.085$) and proliferating $CD8^+$ T subset (C11_CD8_Prolif, $p = 0.061$) than LGG tumors (Figure S2H). Furthermore, when comparing tumor-infiltrating T cell subsets based on tumor-cell- isocitrate dehydrogenase (IDH) mutant status, no significant differences in terms of T cell cluster frequencies were observed between IDH-mutant and wild-type (WT) samples (Figure S2H), consistent with a previous report.[15]

To further verify our observation that glioma-infiltrating T cells were selectively marked with chemokine receptors CCR5 and CXCR3 (Figure 1D), we took advantage of our scRNA-seq data generated from eight paired PBMCs and tumor tissues to examine their mRNA expression in T cells from PBMCs and the TME (Figures S2I and S2J). Consistent with the observations by CyTOF, tumor-infiltrating T cells expressed chemokine receptors *CCR5* and *CXCR3* with higher percentages than those in PBMC samples (Figure S2J). Notably, expressions of *CCR5* and *CXCR3* in tumor-resident T cells were approximately overlapped and mainly confined to tumor-reactive T cell clusters, including CD8_Pre-Ex, CD8_ Ex, CD8_Stress, CD8_Eff, CD4_Dysfun, and CD4_Cyto (Figure S2J). Further analysis revealed that both $CCR5^+CXCR3^+CD4^+$ and $CCR5^+CXCR3^+CD8^+$ T cells in tumors expressed significantly higher levels of effector cytokine genes, including *IFNG* and *TNF*, than their counterparts in PBMCs (Figure S2K). Collectively, our findings highlight that chemokine receptors CXCR3 and CCR5 are required for T cells to migrate into glioma and to execute tumor-killing function.

A unique population of IL-8-producing $CD4^+$ T cells resides in the glioma TME and predicts poor clinical outcomes

Our above T cell atlas has identified a unique $CD4^+$ T subtype that is marked with selective *IL8* expression and enriched exclusively in tumors (Figures 3A and S3A). Similar to the percentage of Treg cells in tumors, this population of IL-8-expressing T cells comprised approximately 10% of the total tumor-infiltrating $CD4^+$ T cells (Figure S2B). Further transcriptome assessment focusing on the $CD4^+$ T cell compartment revealed that IL-8-expressing $CD4^+$ T cells exhibited innate-like features with

(C) The top 10 TCR clones of $CD4^+$ or $CD8^+$ T cells are mapped on a tSNE plot with different colors.
(D) The statistical plots of top 10 clones of $CD4^+$ and $CD8^+$ T cell distribution are shown.
(E) The ordering of $CD4^+$ and $CD8^+$ T cells in a two-dimensional state-space defined by Monocle2.20.
Data in all quantitative panels were analyzed by two-tailed paired t test. *p < 0.05, **p < 0.01, ***p < 0.001, ****p < 0.0001. Cyto, cytotoxicity; Dysfun, dysfunction; Eff, effector; Ex, exhaustion; Prolif, proliferation; Tcm, central memory T cell; Tn-like, naive T cell-like. See also Figure S2 and Tables S3 and S4.

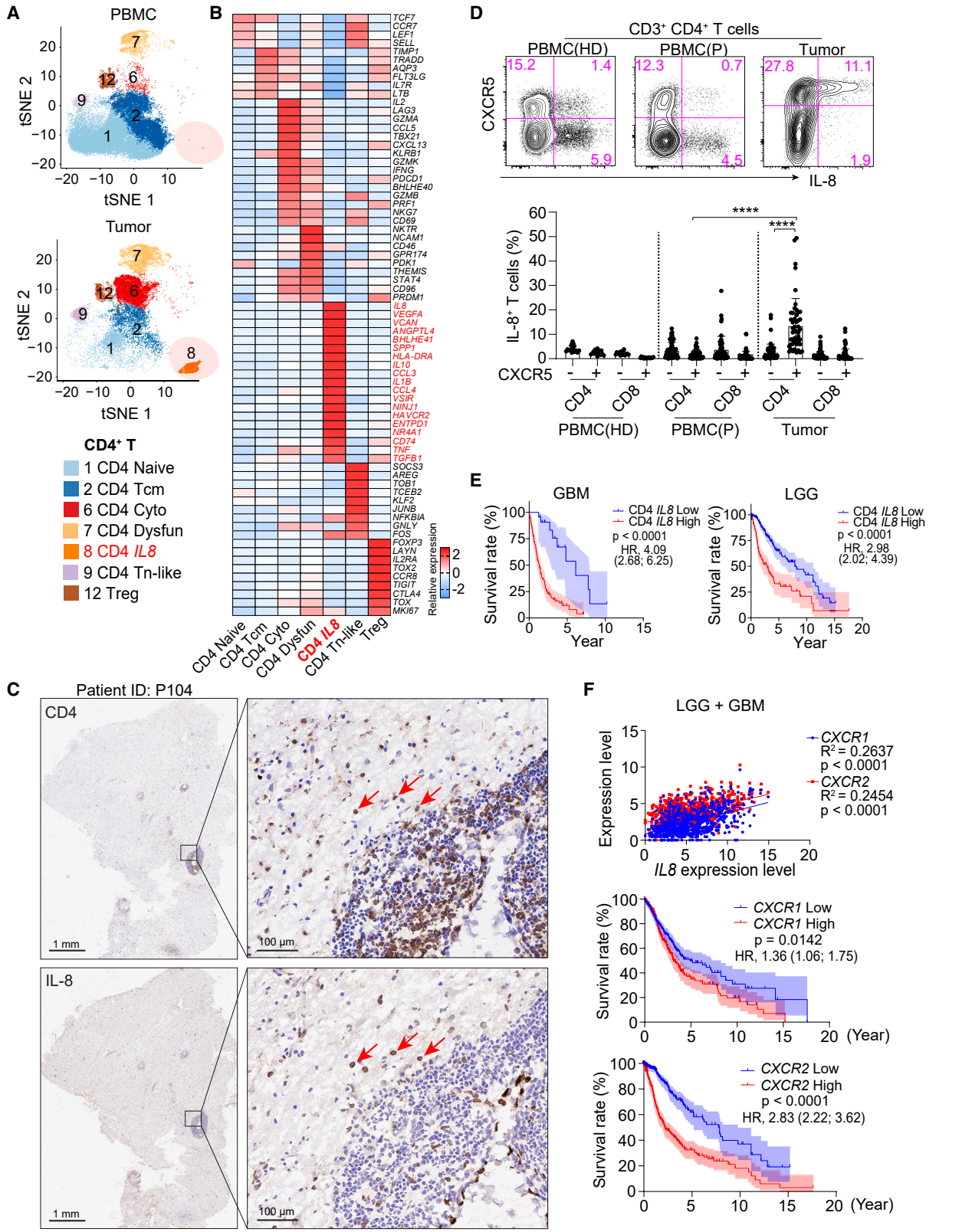

Figure 3. IL-8-producing CD4⁺ T cell subset predicts poor clinical outcome

(A) tSNE plots showing PBMC and tumor-infiltrating CD4⁺ T cells, respectively. The translucent circle shows cluster 8.

(B) Heatmap showing the relative expression of selected genes across CD4⁺ T cell clusters. CD4_*IL8* and its highly expressed genes are highlighted in red.

(legend continued on next page)

substantial expression of classical macrophage-related effector genes, such as *IL8*, *IL1B*, *CCL3* (MIP-1α), *CCL4* (MIP-1β), and myeloid surface marker genes *NINJ1* and *CX3CR1* (Figures 3B and S2C). We then evaluated IL-8, CX3CR1, and NINJ1 protein expression by IHC, immunofluorescence (IF) staining, and flow cytometry and found that IL-8 protein was highly expressed in a fraction of $CD4^+$ T cells that localized around the microvascular zone in glioma, consistent with the general T cell distribution pattern, and these IL-8-producing $CD4^+$ T cells also expressed both CXCR3 and NINJ1 at high levels (Figures 3C, S3B, and S3C). In addition, we performed flow cytometry analysis of T cells in 75 blood and 73 glioma samples from healthy donors and glioma patients and observed that IL-8 was selectively expressed in activated $CXCR5^+$ $CD4^+$ T cells in tumor samples (Figure 3D). Nonetheless, IL-8-expressing T cells in blood were preferentially confined to the $CXCR5^-$ $CD4^+$ T cell population (Figure 3D), indicative of inactivated or naive $CD4^+$ T cells.[24,25]

We next investigated the relevance of the immune properties of the IL-8-producing T cell cluster to clinical outcomes. First, we characterized key signature gene expression levels and designated them as signature scores (Table S5).[26] By integrating the signature score with The Cancer Genome Atlas (TCGA) glioma data, we found a significantly higher signature score of IL-8-producing $CD4^+$ T cells in GBM versus LGG, as well as WT versus IDH-mutant glioma (Figure S3D).[26] A higher signature score of IL-8-producing $CD4^+$ T cells was associated with worse overall survival in both GBM (hazard ratio [HR] [95% confidence interval (CI)] = 4.09 [2.68, 6.25]; $p < 0.0001$) and LGG patients (HR [95% CI] = 2.98 [2.02, 4.39]; $p < 0.0001$) (Figure 3E). However, there was no correlation of survival rate with other clonal T cell subsets (Figure S3E). Furthermore, we extended our analysis and found significant augmentation of *IL8* expression in GBM and IDH-WT compared with LGG and IDH-mutant tumors, respectively (Figure S3F), consistent with a recent study.[27] More importantly, IL-8 expression in glioma was positively correlated with both of its receptors, CXCR1 and CXCR2, which could independently predict poor prognosis in glioma patients (Figure 3F). Collectively, our studies demonstrated a unique population of IL-8-producing $CD4^+$ T cells, which is associated with poor survival of glioma patients.

IL-8-producing T cells differentiated by tumor-secreted stimuli exhibit innate-like features with the capability of promoting tumor growth and myeloid leukocyte recruitment *in vivo*

Pseudotime trajectory analysis of glioma-infiltrating T cells revealed that IL-8 expression was restricted to terminally differentiated and nonclonal $CD4^+$ T cells (Figures 2E and S2F), which is in contrast with spontaneous IL-8 expression in naive $CD4^+$ T cells, especially from children or umbilical cord blood.[24,25,28] We hypothesized that IL-8-producing T cells in glioma are polarized by factors from tumors and are independent of TCR signaling. To test this hypothesis, we sorted human naive $CD4^+$ T cells from healthy donors and subjected them to stimulation with glioma tumor culture supernatant. IL-8 expression in T cells was elevated up to ~55% in a time- and dosage-dependent manner (Figures 4A, S4A, and S4B). Hierarchical clustering analysis based on bulk RNA sequencing data revealed that *in vitro* differentiated IL-8-producing T cells had a similar gene expression pattern to those of the *in vivo* CD4_*IL8* cluster (Figure 4B). Specifically, expression of 2,064 genes (up, 1,487; down, 577) was equivalently changed in both *in vitro* polarized IL-8-producing T cells and the C8_CD4_*IL8* cluster (Figure 4B). Importantly, IL-8-producing T cells expressed transcription factor *BHLHE41* at a high level (Figure S4C), and BHLHE41 was found to be able to bind with its classical consensus site (CACCTGT) located at the upstream conserved non-coding region (CNS) of the *IL8* gene locus (Figures S4D and S4E). Overexpression of BHLHE41 induced substantial expression of IL-8 in human $CD4^+$ T cells, and co-transfer of *BHLHE41*-overexpressed T cells significantly promoted the growth of tumors and shortened mouse survival (Figures S4F–S4I). Further assessment of over 2-fold-changed genes with gene set enrichment analysis (GSEA) and ingenuity pathway analysis (IPA) revealed that IL-8-producing T cells upregulated macrophage-related genes, including *IL-8*, *IL-1B*, *IL-6*, *CCL2*, *CCL3*, *CCL4*, *CCL20*, *CHI3L1*, *CX3CR1*, etc., an innate-like molecular feature similar to those of glioma-associated myeloid cells (Figures 4C and 4D),[29] and might be functionally associated with angiogenesis, monocyte/neutrophil chemotaxis, and oxidation reduction (Figure S4J). These results collectively underscored innate-like $IL\text{-}8^+$ $CD4^+$ T cells as a distinctive $CD4^+$ T effector lineage.

We next sought to determine the function of IL-8-producing $CD4^+$ T cells in glioma. We inoculated U373 cells only into the CNS of immunodeficient mice, or with naive and *in vitro*-generated IL-8-producing $CD4^+$ T cells at a 1:1 ratio, respectively. Mice that received $IL\text{-}8^+CD4^+$ T cells showed significant tumor growth compared with the naive T-bearing mice and control group (Figure 4E). *Ex vivo* analysis of tumor-infiltrating immune cells showed that $CD45^+CD11b^+Gr1^+$ myeloid cells were greatly increased in the $IL\text{-}8^+CD4^+$ T-receiving group compared with the other two groups, and donor $IL\text{-}8^+$ $CD4^+$ T cells constitutively expressed IL-8 at a high level (Figures 4F and 4G). To further verify IL-8-producing T cell function, we adapted another glioma xenograft mouse model by inoculating 20,000 GBM5 cells, a primary glioblastoma cell line described in our very recent study,[30] into immunocompromised mice intracranially (Figure 4H). As shown in Figure 4I, donor IL-8-producing T cells resided closely with

(C) IHC staining of serial neighbor sections of frozen glioma tissue with anti-CD4 or anti-IL-8 antibodies. The red arrow shows CD4 and IL-8 double-positive cells.
(D) IL-8 levels in PBMCs (HD, healthy donor; P, glioma patient) or tumor-infiltrating $CD4^+$ or $CD8^+$ T cells were measured by flow cytometry. Graph data are displayed as the mean ± SD. HD, n = 16; patient PBMC, n = 59; tumor, n = 73. ****$p < 0.0001$, two-tailed unpaired t test.
(E) Kaplan-Meier plots showing the overall survival of GBM and LGG patients from the TCGA database with above (red, high expression; GBM, n = 172; LGG, n = 140) or below (blue, low expression; GBM, n = 23; LGG, n = 377) median expression of the 32-gene signature of CD4_*IL8*. Survival curves are shown with 95% confidence intervals (CIs) as translucent shadows. Hazard ratios (HRs) and their 95% CIs were calculated using stratified Cox proportional hazards regression models, and p values were calculated using a stratified log rank test.
(F) Upper panel, correlation of *IL8* with *CXCR1* (blue) or *CXCR2* (red) in glioma. Middle and lower, survival curves with 95% CIs for glioma patients from the TCGA database with above (red, high expression; n = 292) or below (blue, low expression; n = 396) median expression of *CXCR1* or *CXCR2*.
See also Figure S3 and Table S5.

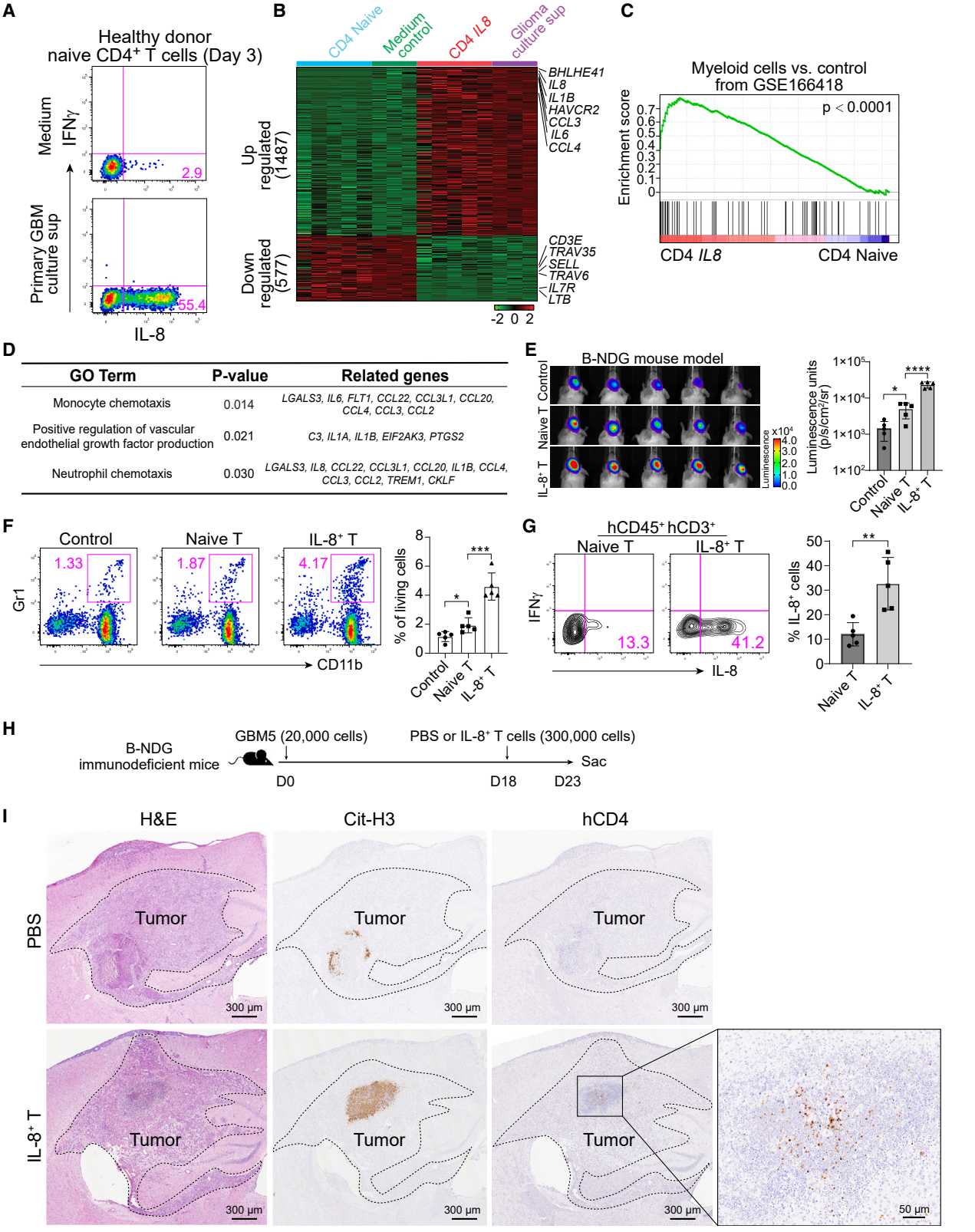

GO Term	P-value	Related genes
Monocyte chemotaxis	0.014	*LGALS3, IL6, FLT1, CCL22, CCL3L1, CCL20, CCL4, CCL3, CCL2*
Positive regulation of vascular endothelial growth factor production	0.021	*C3, IL1A, IL1B, EIF2AK3, PTGS2*
Neutrophil chemotaxis	0.030	*LGALS3, IL8, CCL22, CCL3L1, CCL20, IL1B, CCL4, CCL3, CCL2, TREM1, CKLF*

(legend on next page)

myeloid cells *in situ* and attracted more myeloid cells as compared with the control group. In addition, IL-8$^+$ CD4$^+$ T cells were able to promote angiogenesis both *in vitro* and *in vivo* (Figures S4K and S4L). These results collectively underscored the function of IL-8$^+$ CD4$^+$ T cells in tumors with respect to pro-tumors, chemotaxis for myeloid leukocytes, and pro-angiogenesis.

Given the aforementioned observation that transcriptional factor BHLHE41 played a sufficient role in polarizing IL-8$^+$CD4$^+$ T cells, we next sought to assess its necessary role in these T cells and found that ablation of BHLHE41 by the CRISPR-Cas9 system could not eliminate IL-8 expression in human CD4$^+$ T cells, and adaptive transfer of BHLHE41-knockout CD4$^+$ T cells did not reverse tumor growth and mouse survival in comparison with the scramble control group (data not shown). Therefore, these results indicate that BHLHE41 plays a sufficient, but not necessary, role in programming IL-8-expressing CD4$^+$ T cells.

Expression of IL-8 mainly by tumor, myeloid, and T cells in malignant glioma strengthens the suppressive property of the vascular-immune microenvironment

Accumulating clinical evidence shows that the IL-8 expression level in plasma is positively associated with tumor burden[31] but negatively correlated with the clinical outcome of ICB treatment,[17,18] which leads to the direction of targeting IL-8 and/or its receptor CXCR1/CXCR2 for potential cancer treatment.[32] Nevertheless, because the *IL8* gene is lacking in rodents, the *in vivo* function of IL-8, especially as a key immune regulator in tumorigenesis, remains unclear. We first examined the cellular source of IL-8 production in the context of malignant glioma. The analysis of snRNA-seq data from human GBM (https://portal.gdc.cancer.gov/projects/CPTAC-3)[33] showed that *IL8* expression was mainly confined to tumor, myeloid, and T cells (Figure 5A). Furthermore, we followed the previous strategy[19] and generated an IL-8-humanized (*IL8-Hu*) mouse strain, in which an ~160-kb human BAC clone (RPL11-997L11) containing the entire human *IL8* gene locus and upstream/downstream regulatory elements was inserted into the intergenic region of mouse chromosome 9 (Figure 5B). Consistent with observations from a previous study,[19] naive *IL8-Hu* mice were indistinguishable from WT control mice in terms of appearance, body weight, lifespan, fertility, and immune cell populations in lymph organs (data not shown). We then injected luciferase-expressing GL261 cells into mice intracranially to model human glioblastoma. In comparison with the WT group, *IL8-Hu* mice transplanted with GL261 displayed significantly larger tumor sizes and shorter lifespans (Figure 5C). Histological examination of tumor tissue from *IL8-Hu* mice by IHC and H&E staining showed an increase in tumor necrosis regions and vascular vessel densities, which were frequently accompanied by IL-8-positive polymorphonuclear leukocyte (PMN) infiltrate, in a pattern very similar to that in human GBM tumor tissues (Figures S5A and 5D). More importantly, IL-8 expression was profoundly increased in CD45$^+$CD3$^-$ myeloid and CD4$^+$ T cells in tumors from *IL8-Hu* mice, and these mouse IL-8$^+$CD4$^+$ T cells transcriptionally mirrored human IL-8-expressing CD4$^+$ T cells (Figures 5E and S5B). In addition, tumor-infiltrating CD4$^+$ and CD8$^+$ T cells from *IL8-Hu* mice carried more of the exhaustion markers PD-1 and TIM-3 than those from the control group (Figure 5F). Therefore, in comparison with WT mice, our newly generated *IL8-Hu* mouse strain is more suitable to model human glioma, in which physiological expression of human IL-8 enables the recapitulation of tumor growth acceleration and angiogenesis, as well as the enhancement of myeloid-derived suppressor cell (MDSC) recruitment in the TME.

Blockade of the IL-8-CXCR1/CXCR2 axis synergizes with anti-PD-1 immunotherapy

There is growing awareness that IL-8-enforced immunosuppression remains a hurdle for favorable outcomes of ICB treatment in several tumor types.[16,32,34] By taking advantage of our newly developed *IL8-Hu* mouse model, we sought to explore whether IL-8 is a potential factor accountable for the low efficacy of anti-PD-1 in malignant glioma. We conducted a tumor implantation assay similar to that shown in Figure 5C by intracranially injecting luciferase-expressing GL261 cells into *IL8-Hu* mice. On tumor establishment, tumor-bearing mice were subjected to intraperitoneal (i.p.) administration of anti-PD-1 antibody or isotype IgG. In agreement with previous observations from monotherapy,[35] anti-PD-1 treatment did not show a favorable antitumor response, even though T cell exhaustion in the tumors was significantly alleviated by anti-PD-1 treatment (Figures S5C and S5D). Unexpectedly, the assessment of IL-8 levels in these mice showed that anti-PD-1 treatment significantly enhanced IL-8 expression in both sera and tumor sites compared with the control group (Figures S5E and S5F). Given that human IL-8 is able to chemoattract murine CD11b$^+$ myeloid cells,[36] we analyzed CD11b$^+$

Figure 4. Transcriptional and functional identification of IL-8-producing T cells

(A) Naive CD4$^+$ T cells were cultured with control medium or supernatant from primary glioma cells for 3 days. IL-8 expression was measured by flow cytometry.

(B) Heatmap showing the transcription assessment of control CD4$^+$ T cells (medium control), glioma-culture-supernatant-polarized CD4$^+$ T cells (glioma culture supernatant) from *in vitro* cultures, and CD4_Naive and CD4_*IL8* from scRNA-seq data.

(C) Gene set enrichment analysis (GSEA) measured the enrichment of myeloid cell-related genes in CD4_Naive and CD4_*IL8* clusters.

(D) Gene Ontology (GO) analysis of upregulated genes in both *in vitro* glioma-culture-supernatant-polarized CD4$^+$ T cells and *in vivo* CD4_*IL8* cluster.

(E) *In vivo* bioluminescent imaging of tumor-bearing mice. Human naive CD4$^+$ T cells were cultured as in (A). Then, 50,000 T cells were mixed with 50,000 U373-Luc cells and injected into immunodeficient NOD.CB17-Prkdc^{scid}Il2rg^{tm1}/Bcgen (B-NDG) mice. Fourteen days later, tumor size was measured by *in vivo* bioluminescent imaging.

(F) Flow cytometry analysis of the myeloid cell percentage of tumors in (E).

(G) Flow cytometry analysis of the IL-8 expression in T cells.

(H) Schematic diagram of the experimental approach. Twenty thousand GBM5 cells were implanted into the B-NDG mouse brain. On day 18, 3 μl of PBS or 0.3 million glioma-culture-supernatant differentiated human CD4$^+$ T cells were injected into the tumor. Five days later, mice were sacrificed and analyzed.

(I) H&E or IHC staining with antibody against citrullinated histone H3 (Cit-H3) and human CD4 of tumor tissues.

Data in all quantitative panels are displayed as the mean ± SD. n = 5. *p < 0. 05, **p < 0.01, ***p < 0.001, ****p < 0.0001, two-tailed unpaired t test. hCD4, human CD4; hCD45, human CD45. See also Figure S4.

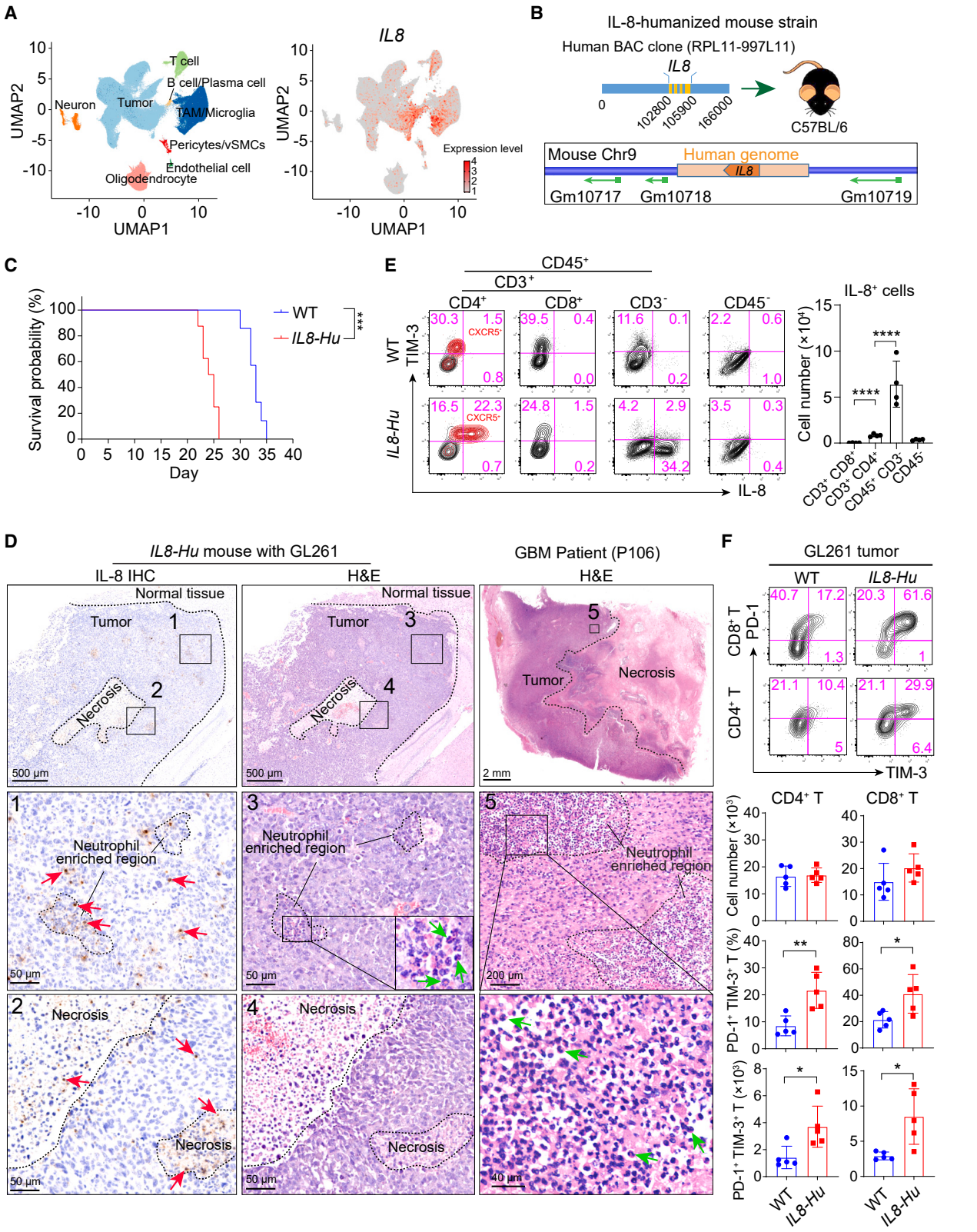

Figure 5. IL-8-humanized mouse strain enables to better model glioma patients' TME

(A) Uniform Manifold Approximation and Projection (UMAP) plot colored by cell types observed in 18 GBM samples. The transcript level of *IL8* is shown on the right.

(legend continued on next page)

myeloid cell populations from the tumor sites and found significant enhancement of two populations of $CD45^+CD11b^{hi}Gr1^{mid}$ and $CD45^+CD11b^{hi}Gr1^{hi}$ MDSCs in anti-PD-1-treated mice compared with the control group, whereas $CD11b^{hi}Gr1^-$ cells, mainly composed of monocyte/microglia and dendritic cells, showed no significant change in cellularity (Figure S5G). Phenotypic characterization of the two populations of MDSCs at the tumor sites defined $CD11b^{hi}Gr1^{mid}$ MDSCs as monocytic (M)-MDSCs signatured with $Ly6C^+$, whereas $CD11b^{hi}Gr1^{hi}$ cells contained both $Ly6G^+$ Granulocytic-myeloid-derived suppressor cells (G-MDSCs) and $Ly6C^+$ M-MDSCs, consistent with previous findings (Figure S5H).[37] In contrast with the tumor sites, only $CD11b^{hi}Gr1^{hi}$ MDSCs (mainly $Ly6G^+$ G-MDSCs) were observed in the spleen, bone marrow, and blood, and they were significantly increased in the bone marrow and blood, but not in the spleen, from anti-PD-1-treated mice in comparison with control mice (Figures S5H and S5I). When assessing IL-8 production in MDSCs, we found that MDSCs from the spleen, blood, and tumor sites, but not from the bone marrow, produced large amounts of IL-8 (Figure S5J), suggesting that MDSCs and IL-8 might play reciprocal roles in facilitating systemic immunosuppression in tumor-bearing mice and cancer patients.[17,38,39] Collectively, these findings demonstrated that anti-PD-1 treatment could increase IL-8 expression and MDSC recruitment systemically, which in turn blunted anti-PD-1 treatment efficacy.

We next investigated whether blockade of the IL-8-CXCR1/CXCR2 axis could potentiate anti-PD-1 efficacy in malignant glioma. Inhibition of CXCR1 and CXCR2 by reparixin, a pharmacological inhibitor,[40] resulted in significantly slower tumor growth and improved survival in both *IL8-Hu* and WT mice (Figures 6A and 6B). Flow cytometry assessment revealed that reparixin treatment abolished not only anti-PD-1-induced but also basal levels of both $CD11b^{hi}Gr1^{hi}$ MDSCs and $CD11b^{hi}Gr1^{mid}$ MDSCs in tumors, but not in spleens, from *IL8-Hu* mice and to a lesser extent from WT mice (Figures 6C, 6D, and S6A). Importantly, the blockade of PD-1, together with reparixin, further reduced Tim-3 and PD-1 expression in T cells to a minimal level, even though the total number of tumor-infiltrating T cells was not significantly changed (Figure 6E). Therefore, our results provide evidence to support the idea that the sequestration of MDSCs by targeting CXCR1 and CXCR2 could leverage anti-PD-1 therapeutic efficacy for glioma.

We next extended our study by examining whether the neutralization of IL-8 has a similar effect. Because human primary glioblastoma cells also express IL-8 at high levels, we stringently modeled human glioblastoma by injecting GL261 cells with dual expression of IL-8 and luciferase into *IL8-Hu* mice, which were then subjected to sequential treatment with PD-1 and/or IL-8 blocking antibodies (Figure 6F). Mice that received anti-IL-8 antibody showed significantly smaller tumor size and improved survival (Figures 6G and 6H). Notably, dual blockade of PD-1 and IL-8 substantially extended the median survival by ~18 days compared with that of the isotype control group (Figure 6H). *Ex vivo* analysis of myeloid cells showed that MDSCs in tumors were nearly depleted by IL-8 neutralization, whereas those in the spleen and deep cervical lymph nodes (the draining lymph nodes for the brain) were mildly affected, consistent with the findings from reparixin-treated mice (Figures S6B–S6D). Dual blockade of PD-1 and IL-8 significantly reduced $PD\text{-}1^{hi}Tim\text{-}3^{hi}$ $CD8^+$ T cells at tumor sites to ~13% versus ~30% in control mice, parallel with the elevation of interferon gamma (IFNγ) production in $CD8^+$ T cells (Figure S6E). In addition, we examined IL-8 production in $CD4^+$ T cells from tumors, spleen, and draining lymph nodes and found that dual blockade of PD-1 and IL-8 significantly increased the percentage, but not the cellularity, of $IL\text{-}8^+CD4^+$ T cells in tumors specifically (Figures S6F and S6G), implying a complementary mechanism for IL-8 production. Given our aforementioned data showing that anti-PD-1 antibody administration augmented systemic IL-8 in *IL8-Hu* mice and the fact that IL-8 is capable of promoting angiogenesis in tumors, we conducted histological assessment of microvascular vessels in glioma tumors by IHC staining of CD31. Compared with control mice, tumor-bearing *IL8-Hu* mice that received anti-PD-1 antibody showed significantly higher microvascular densities, which were then greatly reduced by anti-IL-8 treatment (Figure 6I). Altogether, our findings suggested that the neutralization of IL-8, equivalent to the blockade of its receptors CXCR1 and CXCR2, functions to enhance T cell-mediated antitumor immunity by abolishing suppressive MDSCs.

Blockade of IL-8 reprograms glioma TME

Myeloid cells, including monocyte-derived macrophages (MDMs), microglia, and MDSCs, constitute the main non-neoplastic cellular components in glioma TME.[41,42] We next conducted scRNA-seq analysis to explore the changes in glioma TME in the context of single blockade of PD-1 and IL-8 and combinational blockade. As shown in Figures 7A–7C, unsupervised clustering analysis of scRNA-seq data for $CD45^+$ cells sorted from tumors identified 10 cell sub-types, including microglia, T cell, MDM, M-MDSC, G-MDSC, dendritic cell (DC), activated DC, plasmacytoid DC (pDC), mast cell, and B cell. In agreement with our observation by flow cytometry, more MDSCs were infiltrated into TME of *IL8-Hu* as compared with WT mouse, and anti-PD-1 treatment further enhanced the infiltration of M-MDSCs specifically, whereas IL-8 neutralization eliminated tumor-infiltrating M-MDSCs regardless of anti-PD-1 antibody presence (Figures 7D and 7E). Furthermore, the findings that M-MDSCs were prone to generate reactive oxygen

(B) Schematic representation of IL-8-humanized mouse strain (*IL8-Hu*) construction.
(C) Survival curve of WT and *IL8-Hu* mice bearing GL261 tumors. A total of 10,000 GL261-Luc cells were injected into the callosum and monitored for survival. WT, n = 8; *IL8-Hu*, n = 7. ***p < 0.001, log rank test.
(D) IL-8 IHC and H&E staining of serial sections of GL261 tumors from *IL8-Hu* mice and H&E staining of human tumor tissue. Red arrows show IL-8-positive cells, and green arrows show polymorphonuclear cells.
(E) Flow cytometry analysis of IL-8-producing cells in GL261 tumors of *IL8-Hu* mice. The red color indicates $CXCR5^+$ $CD4^+$ T cells. n = 4.
(F) Flow cytometry analysis of PD-1 and TIM-3 expression on T cells.
Data in all quantitative panels, except for (C), are displayed as the mean ± SD. n = 5, *p < 0. 05, **p < 0.01, ****p < 0.0001, two-tailed unpaired t test. TAM, tumor-associated macrophage; vSMC, vascular smooth muscle cell. Also see Figures S5 and S6.

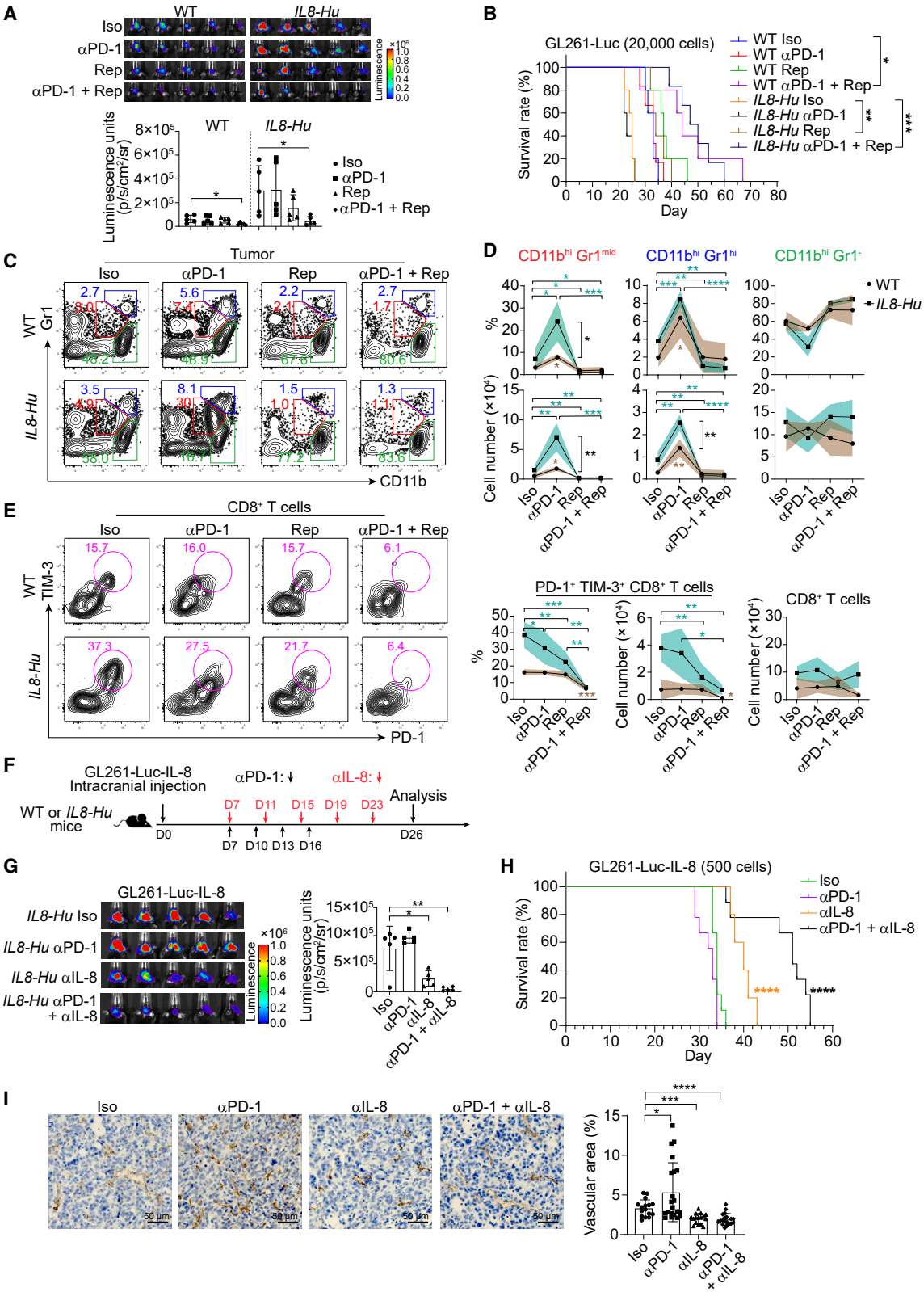

(legend on next page)

species, exemplified with selective expression of fatty acid oxidation-related genes, such as *Alox12e*, *Alox15*, and *Pla2g3*, and superoxide anion generation-related genes, such as *Prg3*, *Tafa4*, and *Nox1* (Figure 7F), highlighted the differential roles of G-MDSCs and M-MDSCs in orchestrating tumor immunosuppressive microenvironment (TIME). In addition, tumor-infiltrating mast cell that is reported to facilitate TIME[43] was nearly depleted by IL-8 neutralization (Figure 7D).

Tumor-associated macrophages (TAMs), including MDMs and microglia, were abundantly enriched in glioma TME of both WT and *IL8-Hu* mice (Figure 7D). To further explore the potential effects on TAMs by IL-8 neutralization, we re-profiled MDM cluster into four sub-clusters, including sub-cluster 1 (type-2-like macrophage, M2-like), sub-cluster 2 (antitumor), sub-cluster 3 (anti-angiogenesis), and sub-cluster 4 (proliferating [prolif]) (Figures 7G and 7H). We found that tumor-infiltrating MDM cells from mice receiving non-anti-IL-8 treatment were mostly (~80%) composed of M2-like macrophage signatured with immune-suppressive and angiogenesis-related genes (Figures 7H and 7I). By contrast, MDM cells from mice treated with anti-IL-8 monotherapy or combinational therapy consisted predominantly of sub-cluster 3, anti-angiogenesis macrophage (Figures 7H, 7I, and S7A). Further pseudotime trajectory analysis implied that M2-like macrophage might give rise to antitumor and anti-angiogenesis macrophage (Figure S7B). Thus, our results demonstrated that neutralization of IL-8 re-programmed MDMs in glioma by switching M2-like to anti-angiogenesis macrophage. Likewise, glioma-resident microglia cells were re-classified into four sub-types, including resting, suppressive, IL-13^{+}, and inflammatory microglia (Figures 7J and 7K). Most strikingly, IL-8 inhibition efficiently ablated suppressive microglia, marked with immunosuppression- and angiogenesis-related genes (Figures 7I, S7A, and S7B).

In summary, our above data demonstrated that IL-8 blockade could re-shape glioma TME from pro-tumor to antitumor status by elimination of both MDSCs and mast cells and repopulation of TAMs, resulting in an overall antitumor immune response in synergy with ICB therapy.

DISCUSSION

We systemically characterized the T cells in human malignant glioma by investigating their anatomic distribution in tumors, heterogeneity at the single-cell level, and functional-state transition from peripheral blood to tumor sites. Our analysis revealed that the majority of T cells at tumor sites were trapped around perivascular regions. These perivascular spaces may serve as default physical barriers to prevent T cells from migrating close to and killing tumor cells. Such a scenario should be considered when constructing new immunotherapy strategies.

CD4^{+} T cells are endowed with a great amount of plasticity to differentiate into distinct subsets affiliated with different effector functions. Very recent studies extended CD4^{+} T cell functions by demonstrating detectable levels of IL-8 expression in T cells from multiple human tissues.[24,25,44] Here, we demonstrated a population of IL-8-producing CD4^{+} T cells that are enriched at tumor sites and differentiated specifically by soluble factors derived by malignant tumor cells in a TCR-independent manner. These cells displayed innate-like features and functionally promoted angiogenesis and MDSC recruitment accompanied by tumor growth. Regardless of these variant observations, our study may further warrant the idea of considering IL-8-producing CD4^{+} T cells as a distinct lineage by the criteria of cytokine production and its related function.

By utilizing our newly developed IL-8-humanized mouse strain, we demonstrated that the IL-8-CXCR1/CXCR2 signaling axis promotes angiogenesis and MDSC recruitment in the glioma TME, which consequentially impedes the ICB-elicited antitumor response. Interestingly, recent clinical data show that the activity of ICB in patients is inversely correlated with IL-8 levels in other tumor types,[17,18] and combinational immunotherapy with anti-PD-1 plus anti-IL-8 exhibits clinical benefit in hepatocellular carcinoma (HCC) patients,[45] providing additional support for our mechanistic discovery that the IL-8-CXCR1/CXCR2 axis plays a pivotal role in governing the immunosuppressive properties of the TME. Importantly, we found that anti-PD-1 administration alone could partially alleviate CD8^{+} T cell exhaustion while augmenting systemic IL-8 expression and the consequential MDSC infiltration, which in turn attenuated ICB efficacy. Systemic elevation of IL-8 by anti-PD-1 treatment might be caused by therapeutic stress, a similar phenomenon found during anti-glioma chemotherapy.[27] In conclusion, we defined a therapeutically

Figure 6. Blockade of the IL-8-CXCR1/CXCR2 axis leverages anti-PD-1 efficacy

(A) *In vivo* bioluminescent imaging of tumor growth. A total of 20,000 GL261-Luc cells were implanted into WT or *IL8-Hu* mouse brains. From day 7, mice were intraperitoneally injected with 200 μg/mouse anti-PD-1 antibody or isotype IgG every 3 days for four times in total. At the same time, a portion of the mice were given 50 μg reparixin by intraperitoneal injection every other day until sacrifice. On day 20, tumor growth was imaged.

(B) Survival curve of mice with different treatments described as in (A). n = 5–6. *p < 0.05, **p < 0.01, ***p < 0.001, log rank test.

(C) Flow cytometry analysis of tumor-infiltrating myeloid cells with Gr1 and CD11b expression on day 21 after tumor injection.

(D) Statistical analysis of the percentage and cell number of CD11b^{hi}Gr1^{mid}, CD11b^{hi}Gr1^{hi}, and CD11b^{hi}Gr1^{-} cells in tumors. 95% CIs are shown in translucent shadows. Brown asterisks show the corresponding significance compared between WT groups, and cyan asterisks show the significance compared between *IL8-Hu* groups. The dark asterisks show the corresponding significance between WT and *IL8-Hu* groups. n = 4.

(E) Flow cytometry analysis of PD-1 and TIM-3 expression on CD8^{+} T cells. n = 4.

(F) Schematic diagram of the experimental approach (G–I). Five hundred GL261-Luc-IL8 cells were implanted into *IL8-Hu* mouse brains. From day 7, mice were administered intraperitoneally with anti-PD-1 antibody and/or anti-IL-8 antibody, as well as isotype control IgG, at a dose of 200 μg/mouse, respectively.

(G) *In vivo* bioluminescent imaging of tumor growth.

(H) Survival curve of the mice with different treatments. n = 9–10. ****p < 0.0001, log rank test.

(I) IHC staining of tumor tissue with antibody against CD31.

Graph data are displayed as the mean ± SD (A, G, and I) or mean ± 95% CI (D and E). *p < 0.05, **p < 0.01, ***p < 0.001, ****p < 0.0001, two-tailed unpaired t test. See also Figure S6.

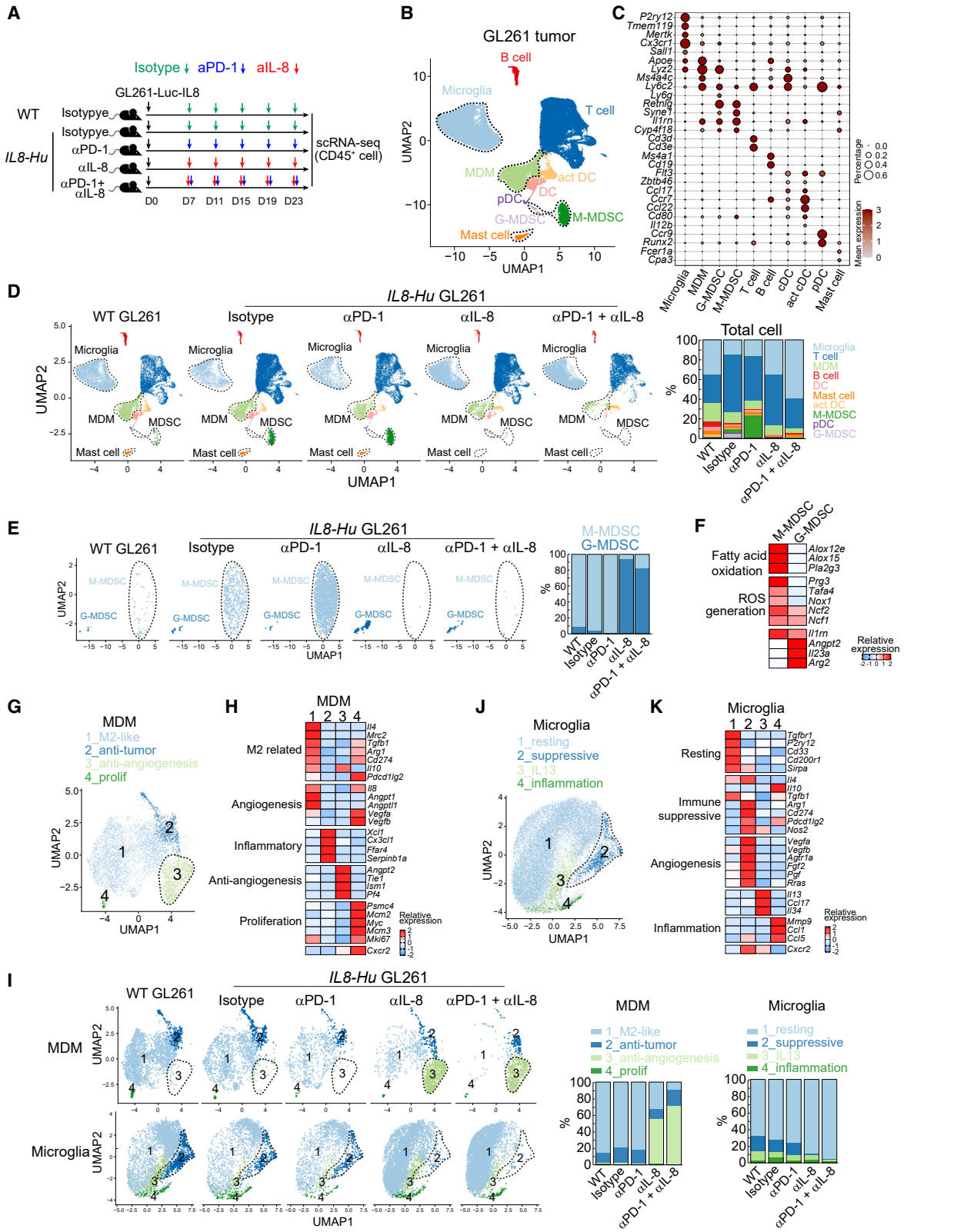

(legend on next page)

targetable chemotaxis axis, and targeting the IL-8/CXCR1/CXCR2 axis in combination with ICB may benefit glioma patients.

STAR★METHODS

Detailed methods are provided in the online version of this paper and include the following:

- KEY RESOURCES TABLE
- RESOURCE AVAILABILITY
  - Lead contact
  - Materials availability
  - Data and code availability
- EXPERIMENTAL MODEL AND SUBJECT DETAILS
  - Human samples
  - Experimental mouse models
  - Glioma cell lines and patient-derived glioma cells
  - Glioma mouse model
- METHOD DETAILS
  - Preparation of cell suspensions from human and mouse tumor tissues
  - scRNA-seq
  - Mass cytometry
  - *In vitro* differentiation of IL-8-producing T cells
  - Cell surface and intracellular cytokine staining for flow cytometry
  - Immunofluorescence (IF) and IHC staining
  - BHLHE41 overexpression in human T cells
  - Chromatin immunoprecipitation quantitative PCR assays (ChIP-qPCR)
  - ELISA
  - Bulk RNA sequencing
  - TCR specificity prediction
  - Tube formation assay
- QUANTIFICATION AND STATISTICAL ANALYSIS
  - Analysis summary
  - scRNA-seq data analysis
  - Mass cytometry data analysis
  - Single-nucleus RNA sequencing (snRNA-seq) data analysis
  - T cell distribution analysis with spatial Ivy Glioblastoma Atlas Project (GAP) data
  - Signature score calculation for T cells clusters
  - Gene set enrichment analysis (GSEA)
  - Statistics

SUPPLEMENTAL INFORMATION

Supplemental information can be found online at https://doi.org/10.1016/j.ccell.2023.03.004.

ACKNOWLEDGMENTS

We thank the members of the Flow Core Facility at the Institute of Pathology and Southwest Cancer Center for their help with cell sorting. We thank Shuaishuai Ding for his help with the graphical abstract drawing. This study was supported by the National Science Foundation of China (31991172, 81821003, and 82192890 to X.B.; 31770973, 82192892, 82171742, and 92259301 to X.L.; 81802866 to Haofei Liu), the joint project of Chongqing Scientific and Technological Commission (2023CCXM001 to X.B.), the Innovation Research Group Project of Chongqing (2019CQSPT16 to X.L.), the Natural Science Foundation Project of Chongqing (CSTB2022TIAD-STX0009 to X.L.), Chongqing Talent Program (cstc2022ycjh-bgzxm0047 to X.L.; cstc2022ycjh-bgzxm0072 to X.W.), and Institute project grants (SWH2015QN07 and SWH2016HWHZ-01 to X.L.).

AUTHOR CONTRIBUTIONS

X.L. and Haofei Liu designed and wrote the manuscript; Haofei Liu, Q.Z., L.T., X.W., R.H., Y.Z., L.C., J.Y., Z.-X.Z., W.R., J.W., Y.F., F.M., P.Z., Xiaoning Zhang, P.Y., W.X., Huimin Lu, Q.L., M.L., C.C., Y.S., Y.-F.P., G.-J.D., X.-H.Y., Z.H., and T.P. helped perform the experiments; L.T. and Z.Y. performed IHC staining of human and mouse tumor samples; Haofei Liu performed scRNA-seq and bulk RNA sequencing; Y.J. performed chromatin immunoprecipitation (ChIP)-PCR; Y.W. and F.H. conducted data analysis; B.Z., Y.C., Xia Zhang, and C.Q. provided important advice; and X.L., X.-W.B., and S.-Q.L. directed the research.

DECLARATION OF INTERESTS

X.L., Haofei Liu, and X.-W.B. have filed a patent on the *IL8-Hu* mouse strain (PCT/CN2022/109093).

Received: May 12, 2022
Revised: June 30, 2022
Accepted: March 2, 2023
Published: March 23, 2023

REFERENCES

1. Aldape, K., Brindle, K.M., Chesler, L., Chopra, R., Gajjar, A., Gilbert, M.R., Gottardo, N., Gutmann, D.H., Hargrave, D., Holland, E.C., et al. (2019). Challenges to curing primary brain tumours. Nat. Rev. Clin. Oncol. *16*, 509–520. https://doi.org/10.1038/s41571-019-0177-5.

Figure 7. Blockade of IL-8 reprograms the tumor immune microenvironment

(A) Schematic diagram of the experimental approach. Five hundred GL261-Luc-IL8 cells were implanted into WT or IL8-Hu mouse brains. On day 7, mice were given isotype antibody, anti-PD-1 antibody, anti-IL-8 antibody, or anti-PD-1 antibody plus anti-IL-8 antibody, intraperitoneally, 200 μg/mouse. Mice were treated with these antibodies every 4 days for a total of five treatments. n = 5.
(B) UMAP plot of immune cells in GL261 tumors.
(C) Bubble chart showing expression levels and expression percentages of marker genes among different cell types.
(D) UMAP plot and stacked bar graph showing profiles of immune cells from indicated groups.
(E) UMAP plots and stacked bar graph showing MDSCs from different groups.
(F) Heatmap showing indicated gene expression in M-MDSCs and G-MDSCs, respectively.
(G) UMAP plot showing sub-clusters in the MDM population.
(H) Heatmap of indicated gene expression in MDM sub-clusters.
(I) UMAP plots and stacked bar graph showing MDMs and microglia from different groups.
(J) UMAP plot showing sub-clusters in the microglia population.
(K) Heatmap of indicated gene expression in microglia sub-clusters.
See also Figure S7.

2. Lim, M., Xia, Y., Bettegowda, C., and Weller, M. (2018). Current state of immunotherapy for glioblastoma. Nat. Rev. Clin. Oncol. *15*, 422–442. https://doi.org/10.1038/s41571-018-0003-5.

3. Quail, D.F., and Joyce, J.A. (2017). The microenvironmental landscape of brain tumors. Cancer Cell *31*, 326–341. https://doi.org/10.1016/j.ccell.2017.02.009.

4. Pombo Antunes, A.R., Scheyltjens, I., Duerinck, J., Neyns, B., Movahedi, K., and Van Ginderachter, J.A. (2020). Understanding the glioblastoma immune microenvironment as basis for the development of new immunotherapeutic strategies. Elife *9*, e52176. https://doi.org/10.7554/eLife.52176.

5. Andersen, B.M., Faust Akl, C., Wheeler, M.A., Chiocca, E.A., Reardon, D.A., and Quintana, F.J. (2021). Glial and myeloid heterogeneity in the brain tumour microenvironment. Nat. Rev. Cancer *21*, 786–802. https://doi.org/10.1038/s41568-021-00397-3.

6. Zheng, L., Qin, S., Si, W., Wang, A., Xing, B., Gao, R., Ren, X., Wang, L., Wu, X., Zhang, J., et al. (2021). Pan-cancer single-cell landscape of tumor-infiltrating T cells. Science *374*, abe6474. https://doi.org/10.1126/science.abe6474.

7. Ren, X., Zhang, L., Zhang, Y., Li, Z., Siemers, N., and Zhang, Z. (2021). Insights gained from single-cell analysis of immune cells in the tumor microenvironment. Annu. Rev. Immunol. *39*, 583–609. https://doi.org/10.1146/annurev-immunol-110519-071134.

8. Klemm, F., Maas, R.R., Bowman, R.L., Kornete, M., Soukup, K., Nassiri, S., Brouland, J.P., Iacobuzio-Donahue, C.A., Brennan, C., Tabar, V., et al. (2020). Interrogation of the microenvironmental landscape in brain tumors reveals disease-specific alterations of immune cells. Cell *181*, 1643–1660.e17. https://doi.org/10.1016/j.cell.2020.05.007.

9. Goswami, S., Walle, T., Cornish, A.E., Basu, S., Anandhan, S., Fernandez, I., Vence, L., Blando, J., Zhao, H., Yadav, S.S., et al. (2020). Immune profiling of human tumors identifies CD73 as a combinatorial target in glioblastoma. Nat. Med. *26*, 39–46. https://doi.org/10.1038/s41591-019-0694-x.

10. Pombo Antunes, A.R., Scheyltjens, I., Lodi, F., Messiaen, J., Antoranz, A., Duerinck, J., Kancheva, D., Martens, L., De Vlaminck, K., Van Hove, H., et al. (2021). Single-cell profiling of myeloid cells in glioblastoma across species and disease stage reveals macrophage competition and specialization. Nat. Neurosci. *24*, 595–610. https://doi.org/10.1038/s41593-020-00789-y.

11. Palma, L., Di Lorenzo, N., and Guidetti, B. (1978). Lymphocytic infiltrates in primary glioblastomas and recidivous gliomas. Incidence, fate, and relevance to prognosis in 228 operated cases. J. Neurosurg. *49*, 854–861. https://doi.org/10.3171/jns.1978.49.6.0854.

12. Jacobs, J.F.M., Idema, A.J., Bol, K.F., Grotenhuis, J.A., de Vries, I.J.M., Wesseling, P., and Adema, G.J. (2010). Prognostic significance and mechanism of Treg infiltration in human brain tumors. J. Neuroimmunol. *225*, 195–199. https://doi.org/10.1016/j.jneuroim.2010.05.020.

13. Heimberger, A.B., Abou-Ghazal, M., Reina-Ortiz, C., Yang, D.S., Sun, W., Qiao, W., Hiraoka, N., and Fuller, G.N. (2008). Incidence and prognostic impact of FoxP3+ regulatory T cells in human gliomas. Clin. Cancer Res. *14*, 5166–5172. https://doi.org/10.1158/1078-0432.CCR-08-0320.

14. Mirzaei, R., Sarkar, S., and Yong, V.W. (2017). T cell exhaustion in glioblastoma: intricacies of immune checkpoints. Trends Immunol. *38*, 104–115. https://doi.org/10.1016/j.it.2016.11.005.

15. Mathewson, N.D., Ashenberg, O., Tirosh, I., Gritsch, S., Perez, E.M., Marx, S., Jerby-Arnon, L., Chanoch-Myers, R., Hara, T., Richman, A.R., et al. (2021). Inhibitory CD161 receptor identified in glioma-infiltrating T cells by single-cell analysis. Cell *184*, 1281–1298.e26. https://doi.org/10.1016/j.cell.2021.01.022.

16. Teijeira, A., Garasa, S., Ochoa, M.C., Villalba, M., Olivera, I., Cirella, A., Eguren-Santamaria, I., Berraondo, P., Schalper, K.A., de Andrea, C.E., et al. (2021). IL8, neutrophils, and NETs in a collusion against cancer immunity and immunotherapy. Clin. Cancer Res. *27*, 2383–2393. https://doi.org/10.1158/1078-0432.CCR-20-1319.

17. Schalper, K.A., Carleton, M., Zhou, M., Chen, T., Feng, Y., Huang, S.P., Walsh, A.M., Baxi, V., Pandya, D., Baradet, T., et al. (2020). Elevated serum interleukin-8 is associated with enhanced intratumor neutrophils and reduced clinical benefit of immune-checkpoint inhibitors. Nat. Med. *26*, 688–692. https://doi.org/10.1038/s41591-020-0856-x.

18. Yuen, K.C., Liu, L.F., Gupta, V., Madireddi, S., Keerthivasan, S., Li, C., Rishipathak, D., Williams, P., Kadel, E.E., 3rd, Koeppen, H., et al. (2020). High systemic and tumor-associated IL-8 correlates with reduced clinical benefit of PD-L1 blockade. Nat. Med. *26*, 693–698. https://doi.org/10.1038/s41591-020-0860-1.

19. Asfaha, S., Dubeykovskiy, A.N., Tomita, H., Yang, X., Stokes, S., Shibata, W., Friedman, R.A., Ariyama, H., Dubeykovskaya, Z.A., Muthupalani, S., et al. (2013). Mice that express human interleukin-8 have increased mobilization of immature myeloid cells, which exacerbates inflammation and accelerates colon carcinogenesis. Gastroenterology *144*, 155–166. https://doi.org/10.1053/j.gastro.2012.09.057.

20. Vita, R., Mahajan, S., Overton, J.A., Dhanda, S.K., Martini, S., Cantrell, J.R., Wheeler, D.K., Sette, A., and Peters, B. (2019). The immune epitope database (IEDB): 2018 update. Nucleic Acids Res. *47*, D339–D343. https://doi.org/10.1093/nar/gky1006.

21. Zheng, C., Zheng, L., Yoo, J.K., Guo, H., Zhang, Y., Guo, X., Kang, B., Hu, R., Huang, J.Y., Zhang, Q., et al. (2017). Landscape of infiltrating T cells in liver cancer revealed by single-cell sequencing. Cell *169*, 1342–1356.e16. https://doi.org/10.1016/j.cell.2017.05.035.

22. Sade-Feldman, M., Yizhak, K., Bjorgaard, S.L., Ray, J.P., de Boer, C.G., Jenkins, R.W., Lieb, D.J., Chen, J.H., Frederick, D.T., Barzily-Rokni, M., et al. (2018). Defining T cell states associated with response to checkpoint immunotherapy in melanoma. Cell *175*, 998–1013.e20. https://doi.org/10.1016/j.cell.2018.10.038.

23. Viegas, C.S.B., Costa, R.M., Santos, L., Videira, P.A., Silva, Z., Araújo, N., Macedo, A.L., Matos, A.P., Vermeer, C., and Simes, D.C. (2017). Gla-rich protein function as an anti-inflammatory agent in monocytes/macrophages: implications for calcification-related chronic inflammatory diseases. PLoS One *12*, e0177829. https://doi.org/10.1371/journal.pone.0177829.

24. Pekalski, M.L., García, A.R., Ferreira, R.C., Rainbow, D.B., Smyth, D.J., Mashar, M., Brady, J., Savinykh, N., Dopico, X.C., Mahmood, S., et al. (2017). Neonatal and adult recent thymic emigrants produce IL-8 and express complement receptors CR1 and CR2. JCI Insight *2*, e93739. https://doi.org/10.1172/jci.insight.93739.

25. Gibbons, D., Fleming, P., Virasami, A., Michel, M.L., Sebire, N.J., Costeloe, K., Carr, R., Klein, N., and Hayday, A. (2014). Interleukin-8 (CXCL8) production is a signatory T cell effector function of human newborn infants. Nat. Med. *20*, 1206–1210. https://doi.org/10.1038/nm.3670.

26. Guo, X., Zhang, Y., Zheng, L., Zheng, C., Song, J., Zhang, Q., Kang, B., Liu, Z., Jin, L., Xing, R., et al. (2018). Global characterization of T cells in non-small-cell lung cancer by single-cell sequencing. Nat. Med. *24*, 978–985. https://doi.org/10.1038/s41591-018-0045-3.

27. Hasan, T., Caragher, S.P., Shireman, J.M., Park, C.H., Atashi, F., Baisiwala, S., Lee, G., Guo, D., Wang, J.Y., Dey, M., et al. (2019). Interleukin-8/CXCR2 signaling regulates therapy-induced plasticity and enhances tumorigenicity in glioblastoma. Cell Death Dis. *10*, 292. https://doi.org/10.1038/s41419-019-1387-6.

28. Crespo, J., Wu, K., Li, W., Kryczek, I., Maj, T., Vatan, L., Wei, S., Opipari, A.W., and Zou, W. (2018). Human naive T cells express functional CXCL8 and promote tumorigenesis. J. Immunol. *201*, 814–820. https://doi.org/10.4049/jimmunol.1700755.

29. Friedrich, M., Sankowski, R., Bunse, L., Kilian, M., Green, E., Ramallo Guevara, C., Pusch, S., Poschet, G., Sanghvi, K., Hahn, M., et al. (2021). Tryptophan metabolism drives dynamic immunosuppressive myeloid states in IDH-mutant gliomas. Nat. Cancer *2*, 723–740. https://doi.org/10.1038/s43018-021-00201-z.

30. Wang, L.H., Yuan, Y., Wang, J., Luo, Y., Lan, Y., Ge, J., Li, L., Liu, F., Deng, Q., Yan, Z.X., et al. (2022). ASCL2 maintains stemness phenotype through

ATG9B and sensitizes gliomas to autophagy inhibitor. Adv. Sci. *9*, e2105938. https://doi.org/10.1002/advs.202105938.

31. Sanmamed, M.F., Carranza-Rua, O., Alfaro, C., Oñate, C., Martín-Algarra, S., Perez, G., Landazuri, S.F., Gonzalez, A., Gross, S., Rodriguez, I., et al. (2014). Serum interleukin-8 reflects tumor burden and treatment response across malignancies of multiple tissue origins. Clin. Cancer Res. *20*, 5697–5707. https://doi.org/10.1158/1078-0432.CCR-13-3203.
32. Bakouny, Z., and Choueiri, T.K. (2020). IL-8 and cancer prognosis on immunotherapy. Nat. Med. *26*, 650–651. https://doi.org/10.1038/s41591-020-0873-9.
33. Wang, L.B., Karpova, A., Gritsenko, M.A., Kyle, J.E., Cao, S., Li, Y., Rykunov, D., Colaprico, A., Rothstein, J.H., Hong, R., et al. (2021). Proteogenomic and metabolomic characterization of human glioblastoma. Cancer Cell *39*, 509–528.e20. https://doi.org/10.1016/j.ccell.2021.01.006.
34. Sanmamed, M.F., Perez-Gracia, J.L., Schalper, K.A., Fusco, J.P., Gonzalez, A., Rodriguez-Ruiz, M.E., Oñate, C., Perez, G., Alfaro, C., Martín-Algarra, S., et al. (2017). Changes in serum interleukin-8 (IL-8) levels reflect and predict response to anti-PD-1 treatment in melanoma and non-small-cell lung cancer patients. Ann. Oncol. *28*, 1988–1995. https://doi.org/10.1093/annonc/mdx190.
35. Song, E., Mao, T., Dong, H., Boisserand, L.S.B., Antila, S., Bosenberg, M., Alitalo, K., Thomas, J.L., and Iwasaki, A. (2020). VEGF-C-driven lymphatic drainage enables immunosurveillance of brain tumours. Nature *577*, 689–694. https://doi.org/10.1038/s41586-019-1912-x.
36. Dominguez, C., McCampbell, K.K., David, J.M., and Palena, C. (2017). Neutralization of IL-8 decreases tumor PMN-MDSCs and reduces mesenchymalization of claudin-low triple-negative breast cancer. JCI Insight *2*, e94296. https://doi.org/10.1172/jci.insight.94296.
37. Gieryng, A., and Kaminska, B. (2016). Myeloid-derived suppressor cells in gliomas. Contemp. Oncol. *20*, 345–351. https://doi.org/10.5114/wo.2016.64592.
38. Movahedi, K., Guilliams, M., Van den Bossche, J., Van den Bergh, R., Gysemans, C., Beschin, A., De Baetselier, P., and Van Ginderachter, J.A. (2008). Identification of discrete tumor-induced myeloid-derived suppressor cell subpopulations with distinct T cell-suppressive activity. Blood *111*, 4233–4244. https://doi.org/10.1182/blood-2007-07-099226.
39. Youn, J.I., Nagaraj, S., Collazo, M., and Gabrilovich, D.I. (2008). Subsets of myeloid-derived suppressor cells in tumor-bearing mice. J. Immunol. *181*, 5791–5802. https://doi.org/10.4049/jimmunol.181.8.5791.
40. Alfaro, C., Teijeira, A., Oñate, C., Pérez, G., Sanmamed, M.F., Andueza, M.P., Alignani, D., Labiano, S., Azpilikueta, A., Rodriguez-Paulete, A., et al. (2016). Tumor-produced interleukin-8 attracts human myeloid-derived suppressor cells and elicits extrusion of neutrophil extracellular traps (NETs). Clin. Cancer Res. *22*, 3924–3936. https://doi.org/10.1158/1078-0432.CCR-15-2463.
41. Hambardzumyan, D., Gutmann, D.H., and Kettenmann, H. (2016). The role of microglia and macrophages in glioma maintenance and progression. Nat. Neurosci. *19*, 20–27. https://doi.org/10.1038/nn.4185.
42. Chryplewicz, A., Scotton, J., Tichet, M., Zomer, A., Shchors, K., Joyce, J.A., Homicsko, K., and Hanahan, D. (2022). Cancer cell autophagy, reprogrammed macrophages, and remodeled vasculature in glioblastoma triggers tumor immunity. Cancer Cell *40*, 1111–1127.e9. https://doi.org/10.1016/j.ccell.2022.08.014.
43. Galli, S.J., Gaudenzio, N., and Tsai, M. (2020). Mast cells in inflammation and disease: recent progress and ongoing concerns. Annu. Rev. Immunol. *38*, 49–77. https://doi.org/10.1146/annurev-immunol-071719-094903.
44. Wong, M.T., Ong, D.E.H., Lim, F.S.H., Teng, K.W.W., McGovern, N., Narayanan, S., Ho, W.Q., Cerny, D., Tan, H.K.K., Anicete, R., et al. (2016). A high-dimensional atlas of human T cell diversity reveals tissue-specific trafficking and cytokine signatures. Immunity *45*, 442–456. https://doi.org/10.1016/j.immuni.2016.07.007.
45. Rossi, A.J., Khan, T.M., Saif, A., Marron, T.U., and Hernandez, J.M. (2022). Treatment of hepatocellular carcinoma with neoadjuvant nivolumab alone versus in combination with a CCR2/5 inhibitor or an anti-IL-8 antibody. Ann. Surg Oncol. *29*, 30–32. https://doi.org/10.1245/s10434-021-10269-7.
46. Dang, W., Xiao, J., Ma, Q., Miao, J., Cao, M., Chen, L., Shi, Y., Yao, X., Yu, S., Liu, X., et al. (2021). Combination of p38 MAPK inhibitor with PD-L1 antibody effectively prolongs survivals of temozolomide-resistant glioma-bearing mice via reduction of infiltrating glioma-associated macrophages and PD-L1 expression on resident glioma-associated microglia. Brain Tumor Pathol. *38*, 189–200. https://doi.org/10.1007/s10014-021-00404-3.
47. Kotecha, N., Krutzik, P.O., and Irish, J.M. (2010). Web-based analysis and publication of flow cytometry experiments. Curr. Protoc. Cytom. *Chapter 10*. Unit10.17. https://doi.org/10.1002/0471142956.cy1017s53.
48. Ding, S., Wu, X., Li, G., Han, M., Zhuang, Y., and Xu, T. (2005). Efficient transposition of the piggyBac (PB) transposon in mammalian cells and mice. Cell *122*, 473–483. https://doi.org/10.1016/j.cell.2005.07.013.
49. Wu, X., Wang, Y., Huang, R., Gai, Q., Liu, H., Shi, M., Zhang, X., Zuo, Y., Chen, L., Zhao, Q., et al. (2020). SOSTDC1-producing follicular helper T cells promote regulatory follicular T cell differentiation. Science *369*, 984–988. https://doi.org/10.1126/science.aba6652.
50. Liu, X., Wang, Y., Lu, H., Li, J., Yan, X., Xiao, M., Hao, J., Alekseev, A., Khong, H., Chen, T., et al. (2019). Genome-wide analysis identifies NR4A1 as a key mediator of T cell dysfunction. Nature *567*, 525–529. https://doi.org/10.1038/s41586-019-0979-8.
51. Shi, Y., Ping, Y.F., Zhou, W., He, Z.C., Chen, C., Bian, B.S.J., Zhang, L., Chen, L., Lan, X., Zhang, X.C., et al. (2017). Tumour-associated macrophages secrete pleiotrophin to promote PTPRZ1 signalling in glioblastoma stem cells for tumour growth. Nat. Commun. *8*, 15080. https://doi.org/10.1038/ncomms15080.
52. Zhang, X.N., Yang, K.D., Chen, C., He, Z.C., Wang, Q.H., Feng, H., Lv, S.Q., Wang, Y., Mao, M., Liu, Q., et al. (2021). Pericytes augment glioblastoma cell resistance to temozolomide through CCL5-CCR5 paracrine signaling. Cell Res. *31*, 1072–1087. https://doi.org/10.1038/s41422-021-00528-3.
53. Shen, X., Wan, C., Ramaswamy, G., Mavalli, M., Wang, Y., Duvall, C.L., Deng, L.F., Guldberg, R.E., Eberhart, A., Clemens, T.L., and Gilbert, S.R. (2009). Prolyl hydroxylase inhibitors increase neoangiogenesis and callus formation following femur fracture in mice. J. Orthop. Res. *27*, 1298–1305. https://doi.org/10.1002/jor.20886.
54. DeCicco-Skinner, K.L., Henry, G.H., Cataisson, C., Tabib, T., Gwilliam, J.C., Watson, N.J., Bullwinkle, E.M., Falkenburg, L., O'Neill, R.C., Morin, A., and Wiest, J.S. (2014). Endothelial cell tube formation assay for the in vitro study of angiogenesis. J. Vis. Exp. e51312. https://doi.org/10.3791/51312.
55. Yao, C., Sun, H.W., Lacey, N.E., Ji, Y., Moseman, E.A., Shih, H.Y., Heuston, E.F., Kirby, M., Anderson, S., Cheng, J., et al. (2019). Single-cell RNA-seq reveals TOX as a key regulator of CD8(+) T cell persistence in chronic infection. Nat. Immunol. *20*, 890–901. https://doi.org/10.1038/s41590-019-0403-4.
56. Trapnell, C., Cacchiarelli, D., Grimsby, J., Pokharel, P., Li, S., Morse, M., Lennon, N.J., Livak, K.J., Mikkelsen, T.S., and Rinn, J.L. (2014). The dynamics and regulators of cell fate decisions are revealed by pseudotemporal ordering of single cells. Nat. Biotechnol. *32*, 381–386. https://doi.org/10.1038/nbt.2859.
57. Puchalski, R.B., Shah, N., Miller, J., Dalley, R., Nomura, S.R., Yoon, J.G., Smith, K.A., Lankerovich, M., Bertagnolli, D., Bickley, K., et al. (2018). An anatomic transcriptional atlas of human glioblastoma. Science *360*, 660–663. https://doi.org/10.1126/science.aaf2666.
58. Guo, X., Zhang, Y., Zheng, L., Zheng, C., Song, J., Zhang, Q., Kang, B., Liu, Z., Jin, L., Xing, R., et al. (2018). Publisher Correction: global characterization of T cells in non-small-cell lung cancer by single-cell sequencing. Nat. Med. *24*, 1628. https://doi.org/10.1038/s41591-018-0167-7.
59. Tirosh, I., Izar, B., Prakadan, S.M., Wadsworth, M.H., 2nd, Treacy, D., Trombetta, J.J., Rotem, A., Rodman, C., Lian, C., Murphy, G., et al.

(2016). Dissecting the multicellular ecosystem of metastatic melanoma by single-cell RNA-seq. Science *352*, 189–196. https://doi.org/10.1126/science.aad0501.

60. Danaher, P., Warren, S., Dennis, L., D'Amico, L., White, A., Disis, M.L., Geller, M.A., Odunsi, K., Beechem, J., and Fling, S.P. (2017). Gene expression markers of tumor infiltrating leukocytes. J. Immunother. Cancer *5*, 18. https://doi.org/10.1186/s40425-017-0215-8.

61. Ritchie, M.E., Phipson, B., Wu, D., Hu, Y., Law, C.W., Shi, W., and Smyth, G.K. (2015). Limma powers differential expression analyses for RNA-sequencing and microarray studies. Nucleic Acids Res. *43*, e47. https://doi.org/10.1093/nar/gkv007.

62. Subramanian, A., Tamayo, P., Mootha, V.K., Mukherjee, S., Ebert, B.L., Gillette, M.A., Paulovich, A., Pomeroy, S.L., Golub, T.R., Lander, E.S., and Mesirov, J.P. (2005). Gene set enrichment analysis: a knowledge-based approach for interpreting genome-wide expression profiles. Proc. Natl. Acad. Sci. USA *102*, 15545–15550. https://doi.org/10.1073/pnas.0506580102.

63. Mootha, V.K., Lindgren, C.M., Eriksson, K.F., Subramanian, A., Sihag, S., Lehar, J., Puigserver, P., Carlsson, E., Ridderstråle, M., Laurila, E., et al. (2003). PGC-1alpha-responsive genes involved in oxidative phosphorylation are coordinately downregulated in human diabetes. Nat. Genet. *34*, 267–273. https://doi.org/10.1038/ng1180.

STAR★METHODS

KEY RESOURCES TABLE

REAGENT or RESOURCE	SOURCE	IDENTIFIER
Antibodies		
anti-human CCR6-141Pr, (Clone G034E3)	Fluidigm	cat# 3141003A, RRID: AB_2687639
anti-human CCR5-144Nd, (Clone NP-6G4)	Fluidigm	cat# 3144007A
anti-human CD8-146Nd, (Clone RPA-T8)	Fluidigm	cat# 3146001, RRID: AB_2687641
anti-human ICOS-151Eu, (Clone C398.4A)	Fluidigm	cat# 3151020B
anti-human CD45RA-153Eu, (Clone HI100)	Fluidigm	cat# 3153001B, RRID: AB_2802108
anti-human CD3-154Sm, (Clone UCHT1)	Fluidigm	cat# 3154003, RRID: AB_2687853
anti-human CXCR3-156Gd, (Clone G025H7)	Fluidigm	cat# 3156004B, RRID: AB_2687646
anti-human CCR4-158Gd, (Clone 205410)	Fluidigm	cat# 3158032A
anti-human CD161-159Tb, (Clone HP-3G10)	Fluidigm	cat# 3159004B
anti-human CD45RO-165Ho, (Clone UCHL1)	Fluidigm	cat# 3165011B, RRID: AB_2756423
anti-human CD25-169Tm, (Clone 2A3)	Fluidigm	cat# 3169003, RRID: AB_2661806
anti-human CXCR5-171Yb, (Clone RF8B2)	Fluidigm	cat# 3171014B, RRID: AB_2858239
anti-human CD4-174Yb, (Clone SK3)	Fluidigm	cat# 3174004, RRID: AB_2687862
anti-human PD-1-175Lu, (Clone EH12.2H7)	Fluidigm	cat# 3175008, RRID: AB_2687629
anti-human CD127-176Yb, (Clone A019D5)	Fluidigm	cat# 3176004, RRID: AB_2687863
anti-human TCR$\gamma\delta$-152SM, (Clone 11F2)	Fluidigm	cat# 3152008B, RRID: AB_2687643
anti-human CD19-142Nd, (Clone HIB19)	Fluidigm	cat# 3142001, RRID: AB_2651155
anti-human CD56-155Gd, (Clone B159)	Fluidigm	cat# 3155008B, RRID: AB_2861412
anti-human CX3CR1-172Yb, (Clone 2A9-1)	Fluidigm	cat# 3172017B
anti-human LAG3-150Nd, (Clone 11C3C65)	Fluidigm	cat# 3150030B
anti-human CD45-BV605, (Clone HI30)	BD Biosciences	cat# 563879, RRID: AB_2744402
anti-human CD45-BV421, (Clone HI30)	BD Biosciences	cat# 563879, RRID: AB_2744402
anti-human CD3-PerCP/Cyanine5.5, (Clone OKT3)	Biolegend	cat# 317336, RRID: AB_2561628
anti-human CD33-PerCP/Cyanine5.5, (Clone P67.6)	Biolegend	cat# 366615, RRID: AB_2566417
anti-human CD45RA-PerCP/Cyanine5.5, (Clone HI100)	Biolegend	cat# 304122, RRID: AB_893357
anti-human HLA-DR-PerCP/Cyanine5.5, (Clone L243)	Biolegend	cat# 307629, RRID: AB_893575
anti-human CD3-PE/Cyanine5, (Clone HIT3a)	Biolegend	cat# 300310, RRID: AB_314046
anti-human CD4-APC, (Clone OKT4)	eBioscience	cat# 17-0048-42, RRID: AB_1963580
anti-human CD44-APC, (Clone HI30)	eBioscience	cat# 17-0459-42, RRID: AB_10667894
anti-human CD4-PE/Cyanine7, (Clone OKT4)	Biolegend	cat# 317414, RRID: AB_571959
anti-human CD45RO-PE/Cyanine7, (Clone UCHL1)	Biolegend	cat# 304230, RRID: AB_11203900
anti-human CD45-PE/Cyanine7, (Clone 2D1)	Biolegend	cat# 368532, RRID: AB_2715892
anti-human CD366 (Tim-3)-APC/Cyanine7, (Clone F38-2E2)	Biolegend	cat# 345025, RRID: AB_2565716
anti-human CD8a-APC/Cyanine7, (Clone HIT8a)	Biolegend	cat# 300926, RRID: AB_10613636
anti-human CD62L-APC, (Clone DREG-56)	Biolegend	cat# 304810, RRID: AB_314470
anti-human IL-8-APC, (Clone E8N1)	Biolegend	cat# 511410, RRID: AB_893464
anti-human CD44-APC, (Clone BJ18)	Biolegend	cat# 338805, RRID: AB_1501202
anti-human CXCR5 (CD185)-Alexa Fluor® 647, (Clone RF8B2)	BD Biosciences	cat# 558113, RRID: AB_2737606
anti-human IL-8-FITC, (Clone E8N1)	Biolegend	cat# 511406, RRID: AB_893462
anti-human CD279 (PD-1)-FITC, (Clone EH12.2H7)	Biolegend	cat# 329904, RRID: AB_940477
anti-human CD14-Alexa Fluor® 488, (Clone M5E2)	BD Biosciences	cat# 557700, RRID: AB_396809
anti-human CD11b-FITC, (Clone ICRF44)	Biolegend	cat# 301330, RRID: AB_2561703
anti-human CD20-FITC, (Clone 2H7)	Biolegend	cat# 302303, RRID: AB_314251
anti-human CD16-Brilliant Violet 421, (Clone 3G8)	Biolegend	cat# 302038, RRID: AB_2561578

(*Continued on next page*)

Continued

REAGENT or RESOURCE	SOURCE	IDENTIFIER
anti-human TCR α/β-FITC, (Clone IP26)	Biolegend	cat# 306706, RRID: AB_314644
anti-human CD14-Pacific Blue, (Clone HCD14)	Biolegend	cat# 325616, RRID: AB_830689
anti-human IL-8 antibody, (polyclonal)	Bio Rad	cat# AHP781, RRID: AB_2264854
anti-human IL-8-PE, (Clone E8N1)	Biolegend	cat# 511408, RRID: AB_893465
anti-human CD197 (CCR7)-APC/Cyanine7, (Clone G043H7)	Biolegend	cat# 353212, RRID: AB_10916390
anti-human Lineage Cocktail (CD3, CD19, CD20, CD56)-APC, (Clone UCHT1; HIB19; 2H7; 5.1H11)	Biolegend	cat# 363601
anti-mouse CD62L-FITC, (clone MEL-14)	BD Biosciences	cat# 553150, RRID: AB_394665
anti-mouse IFN-γ-FITC, (Clone XMG1.2)	BD Biosciences	cat# 554411, RRID: AB_395375
anti-mouse CD4-FITC, (Clone GK1.5)	BD Biosciences	cat# 553729, RRID: AB_395013
anti-mouse TCR β Chain-FITC, (Clone H57-597)	BD Biosciences	cat# 553170, RRID: AB_394683
anti-mouse Ly6G-FITC, (Clone 1A8)	BD Biosciences	cat# 551460, RRID: AB_394207
anti-mouse CD44-FITC, (Clone IM7)	BD Biosciences	cat# 553133, RRID: AB_2076224
anti-mouse CD185 (CXCR5)-Biotin, (Clone 2G8)	BD Biosciences	cat# 551960, RRID: AB_394301
anti-mouse CD4-PE, (Clone GK1.5)	BD Biosciences	cat# 557308, RRID: AB_396634
anti-mouse CD25-PE, (Clone 7D4)	BD Biosciences	cat# 558642, RRID: AB_1645250
anti-mouse I-A/I-E-PE, (Clone M5/114.15.2)	BD Biosciences	cat# 557000, RRID: AB_396546
anti-mouse/human CD11b-PE, (Clone M1/70)	BD Biosciences	cat# 553311, RRID: AB_396680
anti-mouse CD45.2-PE, (Clone 104)	BD Biosciences	cat# 560695, RRID: AB_1727493
anti-mouse CD4-PerCP-Cy™5.5, (Clone RM4-5)	BD Biosciences	cat# 550954, RRID: AB_393977
anti-mouse I-A/I-E-PerCP-Cy™5.5, (Clone M5/114.15.2)	BD Biosciences	cat# 562363, RRID: AB_11153297
anti-mouse/human CD11b-BV510, (Clone M1/70)	BD Biosciences	cat# 562950, RRID: AB_2737913
anti-mouse CD44-APC, (Clone IM7)	BD Biosciences	cat# 559250, RRID: AB_398661
anti-mouse IFN-γ-APC, (Clone XMG1.2)	BD Biosciences	cat# 554413, RRID: AB_398551
anti-mouse CD279 (PD-1)-FITC, (Clone J43)	eBioscience	cat# 11-9985-82, RRID: AB_465472
anti-mouse CD45-PE, (Clone 30-F11)	eBioscience	cat# 12-0451-82, RRID: AB_465668
anti-mouse Ly6C-PerCP-Cyanine5.5, (Clone HK1.4)	eBioscience	cat# 45-5932-80, RRID: AB_2723342
anti-mouse CD62L-PE, (Clone MEL-14)	Biolegend	cat# 104408, RRID: AB_313095
anti-mouse CD279 (PD-1)-PE/Cyanine7 (Clone RMP1-30)	Biolegend	cat# 109110, RRID: AB_572017
anti-mouse Ly6G/Ly6C (Gr-1)-PerCP/Cyanine5.5, (Clone RB6-8C5)	Biolegend	cat# 108428, RRID: AB_893558
anti-mouse CD223 (LAG-3)-PerCP/Cyanine5.5, (Clone C9B7W)	Biolegend	cat# 125212, RRID: AB_2561517
anti-mouse CD366 (Tim-3)-Brilliant Violet 421™, (Clone RMT3-23)	Biolegend	cat# 119723, RRID: AB_2616908
anti-mouse/human CD11b-APC, (Clone M1/70)	Biolegend	cat# 101212, RRID: AB_312795
anti-mouse/human CD44-APC/Cyanine7, (Clone IM7)	Biolegend	cat# 103028, RRID: AB_830785
anti-mouse/human CD31, (polyclonal)	Abcam	cat# ab28364, RRID: AB_726362
anti-human CD4, (Clone EPR6855)	Abcam	cat# ab133616
anti-mouse/human Histone H3 (citrulline R2 + R8 + R17), (polyclonal)	Abcam	cat# ab5103
Goat anti-rabbit IgG (H+L) secondary antibody, Alexa Fluor 647	Thermo	cat# A-21245, RRID: AB_2535813
human IL-8/CXCL8 Antibody, (Clone 6217)	R&D	cat# MAB208
human TruStain FcX™ (Fc Receptor Blocking Solution)	Biolegend	cat# 422302, RRID: AB_2818986
Anti-mouse/human BHLHE41, (clone 2135CT82.1.84)	Thermo	cat# MA5-37787, RRID: AB_2897711
InVivoPlus anti-Mouse PD-1 (CD279), (Clone RMP1-14)	Bio X Cell	cat# BP0146
Biological samples		
Human blood and tumor samples	Biobank of Southwest Hospital, Third Military Medical University, Chongqing, China	N/A

(*Continued on next page*)

Continued

REAGENT or RESOURCE	SOURCE	IDENTIFIER
Chemicals, peptides, and recombinant proteins		
Cisplatin	Sigma	cat# P4394
MAXPAR water	Fluidigm	cat# 201069
Maxpar® Cell Staining Buffer	Fluidigm	cat# 201068
Maxpar® Fix and Perm Buffer	Fluidigm	cat# 201067
Cell-ID™ Intercalator-Ir—125 μM	Fluidigm	cat# 201192A
Zombie Violet™ Fixable Viability Kit	Biolegend	cat# 423113
Streptavidin-PE	SouthernBiotech	cat# 7105-09M
Allophycocyanin (APC) Streptavidin	Jackson ImmunoResearch	cat# 016-130-084, RRID: AB_2337242
VivoGlo™ Luciferin, *In Vivo* Grade	Promega	cat# P1043
phorbol 12-myristate 13-acetate (PMA)	Sigma	cat# P1585
Ionomycin	Sigma	cat# 407953
Reparixin	MCE/MedChem Express	cat# HY-15251
Cytiva Percoll™ Centrifugation Media	Fisher scientific	cat# 10607095
Ficoll-Paque PLUS	GE Healthcare	cat# 17-1440-03
Recombinant Human EGF Protein, CF	R&D	cat# 236-EG
Recombinant Human FGF basic/FGF2/bFGF (146 aa) Protein	R&D	cat# 233-FB
B-27 Supplement	Thermo	cat# 17504044
EGM™ Endothelial Cell Growth Medium	Lonza	cat# CC-3129
Neurobasal™-A Medium (1X) Liquid without Phenol Red	Thermo	cat# 12349015
X-vivo 20 Hematopoietic Serum-Free Culture Media	Lonza	cat# BW04-448Q
Critical commercial assays		
Fixation/Permeabilization Solution Kit with BD GolgiPlug™	BD Biosciences	cat# 555028, RRID: AB_2869013
Pan T Cell Isolation Kit, human	Miltenyi Biotec	cat# 130-096-535
Dynabeads Mouse T-Activator CD3/CD28	Thermo	cat# 11452D
Dynabeads Human T-Activator CD3/CD28	Thermo	cat# 11131D
Deposited data		
Human scRNA-Seq data	This paper	PRJCA013123, OMIX002375
Human bulk RNA sequencing data	This paper	PRJCA013123, OMIX002390
Mouse scRNA-Seq data	This paper	PRJCA013123, OMIX002376
Mouse bulk RNA sequencing data	This paper	PRJCA013123, OMIX002391
Experimental models: Cell lines		
GL261	Dang et al.[46]	N/A
GL261-Luc	This paper	N/A
GL261-Luc-IL8-RFP	This paper	N/A
GL261-OVA-Luc	This paper	N/A
Experimental models: Organisms/strains		
IL8-Hu mice	This paper	N/A
B-NDG mice	Biocytogen	Cat# 110586
C57BL/6J mice	Vitalriver	Cat# 219
Oligonucleotides		
ChIP-qPCR primers, see Table S6	This paper	N/A
sgRNA sequences, see Table S7	This paper	N/A
Software and algorithms		
FlowJo v10.2	BD Biosciences	https://www.flowjo.com/
Cytobank	Kotecha et al.[47]	https://www.cytobank.org/
Living Image®4.5.2	Caliper LifeScience	https://www.perkinelmer.com.cn/
ImageJ 1.46r	NIH, Bethesda, MD	https://imagej.nih.gov/ij/
GraphPad Prism	GraphPad	https://www.graphpad.com/

RESOURCE AVAILABILITY

Lead contact

Requests for further information should be directed to Xindong Liu (Xindongliu@hotmail.com).

Materials availability

Requests for resources and reagents should be directed to and will be fulfilled by Xindong Liu (Xindongliu@hotmail.com).

Data and code availability

scRNA-seq and bulk RNA sequencing data have been deposited at the National Genomics Data Centre of China (https://ngdc.cncb.ac.cn/) under accession number PRJCA013123 (Human scRNA-Seq data: OMIX002375, Human bulk RNA sequencing data: OMIX002390, Mouse scRNA-Seq data: OMIX002376, and Mouse bulk RNA sequencing data: OMIX002391) and are publicly available as of the date of publication.

This paper does not report original code.

Any additional information required to reanalyze the data reported in this paper is available from the lead contact upon request.

EXPERIMENTAL MODEL AND SUBJECT DETAILS

Human samples

Surgically resected glioma samples were provided on ice within 30 minutes of lesion excision. Patients' blood samples were obtained the day before surgery. All human samples used in this study were approved by the ethics committees of Third Military Medical University (TMMU), with informed consent from patients or their guardians. Clinical information related to patients was summarized in Table S1. Glioma patients included both females (n = 59) and males (n = 93) spanning a range of ages from 16 to 80 years. 163 samples (82 tumor samples, 62 blood samples from patients, and 19 blood samples from healthy donors) were subjected to flow cytometry analysis, 8 PBMCs and 12 tumor tissues were subjected to scRNA-seq, 19 samples (14 tumor samples and 5 blood samples from patients) were subjected to mass cytometry analysis, 72 tumor samples were subjected to immunofluorescence or immunohistochemistry analysis, 6 tumor samples were subjected to adherent cell culture.

Experimental mouse models

*IL-8 humanized (*IL8-Hu*) mouse strain generation*

The *IL8-Hu* mouse strain was constructed as previously described.[19] Briefly, PiggyBac-on-BAC RP11-997L11, which contains the human *IL8* locus, was inserted into the C57BL/6 mouse genome. Four pairs of BAC-specific primers that amplified 300–800 bp fragments from different parts of the BAC plasmid were used to identify BAC-positive pups by PCR analysis. Offspring carrying the intact human *IL8* gene locus were back-crossed with C57BL/6 mice for 5 generations. Inverse PCR was used to identify the *IL8* insertion site as previously described.[48] Briefly, genomic DNA was extracted from tails, digested with HaeIII (NEB, Cat# R0108S), and then ligated with T4 DNA Ligase (NEB, Cat# M0202L). The primers used to recover the flanking sequence of the left side of the PiggyBac transposon were PB-5IF (5′-CTTGACCTTGCCACAGAGGACTATTAGAGG-3′) and PB-5IR (5′-CAGTGACAC TTACCGCATTGACAAGCACGC-3′). The primers used to recover the flanking sequence of the right side of the piggyBac transposon were PB-3IF (5′-CCTCGATATACAGACCGATAAAACACATGC-3′) and PB-3IR (5′-AGTCAGTCA GAAACAACTTTGGCACATATC-3′). PCR products were cloned into pMD19-T (Sino Biological) for subsequent sequencing. Sequencing results were analyzed with NCBI BLAST searches (www.ncbi.nlm.nih.gov) and ensemble human and mouse genome databases (www.ensembl.org). All mice used in this study were kept in individually ventilated cages under specific-pathogen-free condition, and all mouse protocols were approved by the ethics committees of TMMU.

Glioma cell lines and patient-derived glioma cells

GL261 (provided kindly by Prof. Zi-ling Wang)[46] and U373 cells (European Collection of Authenticated Cell Cultures (ECACC), Cat# 08061901) were transfected with lentivirus carrying *Luc-GFP*, and GFP-positive cells were sorted by flow cytometry to generate a luciferase-stable cell line. To establish an IL-8-producing cell line, IL8 was overexpressed in GL261-Luc cells using lentivirus carrying IL8-RFP, and RFP-positive cells were sorted by flow cytometry. Cells were maintained *in vitro* with DMEM supplemented with 10% fetal bovine serum (FBS) (Gibco, Cat# 10099), 2 mM GlutaMAX, and 100 U/mL penicillin/streptomycin. GBM5 were cultured in ultra-low attachment dishes (Corning, Cat# 3262) using neurobasal medium (Gibco, Cat# 12349015) supplemented with 2% B-27 (Gibco, Cat# 12587010), 100 U/mL penicillin/streptomycin, 1.5% GlutaMAX (Life Technology, Cat# 35050-061), Mem nonessential anions (Life Technology, Cat# 11140-050), 10 ng/mL EGF (Peprotech, Cat# AF-100-15) and 10 ng/mL FGF-basic (Peprotech, Cat# AF-100-17A). For adherent cell culture, cells were cultured with DMEM/F-12 medium (Gibco, Cat# 11320033) containing 10% FBS in adhesive dishes (Thermo, Cat# 150460). All tumor cell lines were tested monthly for mycoplasma and cultured at 37°C with 5% CO_2.

Glioma mouse model

Tumor cells were injected as previously described with minor modifications.[35] For the GL261 tumor model, C57BL/6 or *IL8-Hu* mice (8–12 weeks old; 3–10 mice per group) were anesthetized using a mixture of ketamine (50 mg/kg) and xylazine (5 mg/kg) injected

intraperitoneally. Mouse heads were shaved and then placed in a stereotaxic frame. After the sterilization of the scalp with alcohol and betadine, a 1-centimeter midline scalp incision was made to expose the skull. Then, 4% H_2O_2 was used to remove the periosteum, and a burr hole was drilled 2 mm lateral and 1 mm posterior from the bregma. A 10 μL syringe (Hamilton, 1701 RN no NDL) with a 33 G needle was injected at a depth of 2 millimeters (mm) and retracted 0.5 mm to form a reservoir. Using a microinfusion pump, tumor cells were injected in a volume of 3 μL at a speed of 1 μL/minute. The syringe was left in place for 1 minute before removal of the syringe. Bone wax was used to fill the burr hole, and the skin was conglutinated and cleaned. Mice were placed in a heated cage until full recovery. GBM5, U373-Luc, or U373-Luc plus T cells were injected into 6–8-week-old B-NDG mice (NOD. CB17-Prkdc^{scid}Il2rg^{tm1}/Bcgen, Biocytogen, China) as described above, with 5–7 mice per group. To measure tumor growth, tumor-bearing mice were anesthetized using isoflurane intraperitoneally and injected intraperitoneally with D-Luciferin (150 mg/kg body weight; Promega, Cat# P1043). After 10 minutes, the animals were transferred to the IVIS 100 imaging system (Caliper Life Sciences), and luminescence was detected. Data were subsequently analyzed using Living Image 2.5 software (Caliper Life Sciences).

METHOD DETAILS

Preparation of cell suspensions from human and mouse tumor tissues

Fresh resected tumor samples were put on ice and taken within 2 hours to the laboratory to start dissection and processing. First, tissue samples were thoroughly washed with precooled PBS on ice to remove visible blood clots. Then, tumor samples were mechanically disrupted into small pieces with a sterile scalpel and further dissociated into single-cell suspensions using a brain tumor dissociation kit (Miltenyi Biotec, Cat# 130-095-942) following the manufacturer's protocol. Afterward, the homogenate was filtered through a 70 μm strainer and centrifuged at 500 × g for 10 minutes at 4°C. This was followed by an immune cell enrichment step using density gradient centrifugation with 30% and 70% Percoll (Fisher Scientific, Cat# 10607095) in RPMI 1640 medium containing 10% FBS. After centrifuge at 2000 × g for 20 minutes at 20°C (without brakes during acceleration and deceleration), the middle transparent layer containing immune cells was collected. After washing with PBS containing 1.5% FBS and 20 mM EDTA, the cells were ready for flow cytometry analysis or sorting. For mouse tumor, tumor tissue was cut into pieces and incubated in C-Tubes (Miltenyi Biotec, Cat# 130-096-334) with digestion cocktail containing 1 mg/mL collagenase D (Roche, Cat# 11088882001) and 30 μg/mL DNase I (Sigma–Aldrich, Cat# D7291-2MG) in complete RPMI 1640 medium (10% FBS) at 37°C for 15 minutes and then dissociated on gentleMACS with Program m_brain_01 followed by incubation for another 15 minutes at 37°C. Afterward, the homogenate was filtered through a 70 μm strainer and centrifuged at 500 × g for 10 minutes at 4°C. Then, gradient centrifugation was carried out as described above.

scRNA-seq

Percoll-enriched human immune cells or PBMCs were stained with Zombie dye (Biolegend, Cat# 423113). After blocking with Human TruStain FcX (Biolegend, Cat# 422302) at 4°C for 15 min, the cells were stained with antibodies against CD45 and CD3 for 30 min at 4°C. Human T cells were sorted by gating on Zombie dye$^-$ CD45$^+$ CD3$^+$ single cells. The scRNA-seq libraries were generated using the Chromium Single Cell 3′ Library and Bead Kit v.2 (10x Genomics) as previously described.[49] Briefly, 10,000–20,000 live cells were used to generate single-cell gel beads in an emulsion. Gel beads in the emulsion were disrupted post reverse transcription. Barcoded complementary DNA was isolated and amplified by PCR. Following fragmentation, end repair and A-tailing, sample indices were added during index PCR. The purified libraries were sequenced on a NovaSeq 6000 System (Illumina).

Percoll-enriched mouse immune cells from GL261 tumor were stained with Zombie dye (Biolegend, Cat# 423113). After blocking with anti-mouse CD16/32 (Biolegend, Cat# 163403) at 4°C for 15 min, the cells were stained with antibodies against mouse CD45 for 30 min at 4°C. Immune cells were sorted by gating on Zombie dye$^-$ CD45$^+$ single cells. scRNA-seq libraries were prepared using SeekOne® MM Single Cell 3′ library preparation kit (SeekGene Cat# SO01V3.1). Briefly, 20,000 cells were loaded into the flow channel of SeekOne® MM chip which had 170,000 microwells and allowed to settle in microwells by gravity. After removing the unsettled cells, Cell Barcoded Magnetic Beads (CBBs) were pipetted into flow channel and allowed to settle in microwells with the help of a magnetic field. Next excess CBBs were rinsed out and cells in MM chip were lysed to release RNA which was captured by the CBB in the same microwell. Then all CBBs were collected and reverse transcription were performed at 37°C for 30 minutes to label cDNA with cell barcode on the beads. Exonuclease I was used to remove unused primer on CBBs. Subsequently, barcoded cDNA on the CBBs was hybridized with random primer which had SeqPrimer sequence on the 5′ end. The amplified cDNA product was then cleaned to remove unwanted fragment and added to full length sequencing adapter and sample index by indexed PCR. The indexed sequencing libraries were cleanup with SPRI beads, quantified by quantitative PCR (KAPA Biosystems, Cat# KK4824) and then sequenced on NovaSeq 6000.

Mass cytometry

Three million Percoll-enriched cells were stained with 0.5 μM cisplatin in 1 mL PBS (without Ca^{2+} and Mg^{2+}) for 2 minutes at room temperature. Two mL Cell Staining Buffer (Fluidigm, Cat# 201068) were added to stop the reaction, and the mixture was centrifuged at 500 × g for 5 minutes. After Fc blocking (Biolegend, Cat# 422302), the cells were stained with a metal-labeled antibody cocktail containing 16 antibodies (CCR6-141Pr, CCR5-144Nd, CD8-146Nd, CD45RA-153Eu, CD3-154Sm, CXCR3-156Gd, CCR4-158Gd, CD45RO-165Ho, CD25-169Tm, CD4-174Yb, PD-1-175Lu, TCRγδ-152SM, CD19-142Nd, CD56-155Gd, CX3CR1-172Yb, LAG3-150Nd) at room temperature for 30 minutes. After washing with Cell Staining Buffer, cells were stained with 125 μM Intercalator-Ir

(Fluidigm, Cat# 201192A) in Fix and Perm Buffer (Fluidigm, Cat# 201067) for 1 hour at room temperature. Then, cells were washed with Maxpar® water (Fluidigm, Cat# 201069) twice, mixed with EqBeads (Fluidigm, Cat# 201078) and analyzed on a CyTOF Helios machine.

In vitro differentiation of IL-8-producing T cells

Naïve ($CD3^+$ $CD4^+$ $CD45RA^+$ $CCR7^+$ $CD45RO^-$) and effector/memory ($CD3^+$ $CD4^+$ $CD45RA^-$ $CCR7^-$ $CD45RO^+$) T cells from healthy donors were FACS-sorted and cultured with X-VIVO 20 medium (Lonza, Cat# BW04-448Q) containing 50% primary glioma supernatant for 3 days. Then, IL-8 expression was measured by flow cytometry. For *in vivo* experiment, *in vitro* cultured naïve T cells were mixed with human glioma cells (tumor cells: T cells = 1:1) and injected into the B-NDG mouse brain. For transcription factor overexpression assay, Jurkat cells were infected with lentiviruses JUN-LV-GFP, FOS-LV-GFP, FOSB-LV-GFP, ATF3-LV-GFP, Dec2-LV- GFP, DDIT3-LV-GFP, MAFB-LV-GFP, NRIP3-LV-GFP, TCEAL7-LV-GFP, ELF1-LV-GFP or empty vector for 2 days, followed with IL-8 expression analysis by flow cytometry.

Cell surface and intracellular cytokine staining for flow cytometry

Cell surface and intracellular staining were performed as previously described.[50] Briefly, cells from various experiments were stained with fluorescence-labeled antibody cocktails for 30 minutes at 4°C and then analyzed with a BD LSRFortessa instrument. To measure cytokine expression in lymphocytes, cells were stimulated with 100 ng/mL phorbol-12-myristate-13-acetate (PMA) and 1 μg/mL ionomycin in the presence of GolgiPlug (BD Biosciences, Cat# 555028) for 5 hours. Intracellular staining was carried out with a Fixation/Permeabilization Kit (BD Biosciences, Cat# 555028). Data were analyzed with FlowJo.

Immunofluorescence (IF) and IHC staining

IF staining was performed as previously described.[51] Alexa Fluor® 488-labeled anti-human CD4 antibody (Biolegend, Cat# 317420, 1:200 dilution), rabbit anti-human IL-8 antibody (Bio-Rad, Cat# AHP781, 1:500 dilution), and Alexa Fluor® 674-labeled goat anti-rabbit secondary antibody (Thermo, Cat# A-21245, 1:200 dilution) were used to show CD4- and IL-8-positive cells in frozen glioma sections. Images were collected with a Zeiss LSM 900. IHC staining was carried out according to the methods described previously with minor modifications.[52] Briefly, formalin-fixed paraffin-embedded tumor tissue blocks, or frozen tumor tissues were cut into 3 μm-thick serial sections. After blocking with streptavidin peroxidase, heat-induced antigen epitope retrieval in citrate buffer (pH: 6.0) was performed. Sections were incubated overnight at 4°C with primary antibodies against Cit-H3 (Abcam, Cat# ab5103, 1:300 dilution), CD31 (Abcam, Cat# ab28364, 1:200 dilution), IL-8 (Bio–Rad, Cat# AHP781, 1:1000 dilution) or CD4 (Abcam, Cat# ab133616, 1:200 dilution) followed by counterstaining with hematoxylin. Staining was visualized by a Dako REAL™ EnVision™ Detection System (Dako, Cat# K5007), and sections were scanned with Axio Scan.Z1 (ZEISS). Quantitative analysis of CD31- and IL-8-positive regions or IL-8-positive spots was performed using ImageJ 1.46r as previously described.[53] The images were converted to RGB stacks, and thresholding was used to measure the pixel area or particles of CD31 and IL-8 staining by a blinded observer. In this context, 3–10 randomly selected visual fields (200× magnification) of each tumor were analyzed.

BHLHE41 overexpression in human T cells

Human naïve $CD4^+$ T cells were sorted from PBMCs of healthy donors. Naïve $CD4^+$ T cells were activated with plate-bound anti-human CD3/CD28 for 24 hours. T cells were transduced with control lentiviruses or lentiviruses encoding BHLHE41 (BHLHE41-LV-GFP). Eight μg/mL of polybrene was added to each well. Plates were sealed and then spun at 1,000 × g at 30°C for 90 min. Three days later, GFP positive cells were sorted and were ready for further analysis.

Chromatin immunoprecipitation quantitative PCR assays (ChIP-qPCR)

ChIP-qPCR was performed as described previously.[50] Briefly, naïve $CD4^+$ T cells were sorted from PBMC of healthy donors and infected with lentivirus BHLHE41-HA-LV-GFP. GFP positive cells were sorted and fixed by 1% paraformaldehyde, and this was followed by digestion with Mnase cocktail (Active motif, Cat# 53035). Chromatin from 5×10^6 cells was used for each ChIP experiment. Antibodies against HA tag (CST, Cat# 3724) and IgG isotype were used. The final DNA extracts were amplified with qPCR. The values from the immunoprecipitated samples were normalized to that from the input DNA. Primer sequences were listed in Table S6.

ELISA

To detected IL-8 level in humanized mice, 96-well plate (Thermo, Cat# 442404) was coated with 5 μg/mL IL-8 capture antibody (Biolegend, Cat# 514602) at 4°C overnight. After blocking with 1% BSA for 1 hour, mouse serum or standard substance (Biolegend, Cat# 570909) was incubated at 4°C overnight. After washing, 2 μg/mL biotin-labeled detection antibody (Biolegend, Cat# 514704) was added and incubated at room temperature for 1 hour, followed by another one-hour incubation with streptavidin-HRP (R&D, Cat# DY998). IL-8 concentration was quantified with HRP-catalyzed oxidation of o-phenylenediamine (Sigma, Cat# P8936) and measured by a MULTISKAN GO instrument (Thermo Scientific).

Bulk RNA sequencing

Total RNA was extracted using TRIzol reagent (Invitrogen, Cat# 15596026). RNA library preparation was conducted by using the NEBNext Ultra RNA Library Prep Kit for Illumina (New England Biolabs) according to the manufacturer's protocols. After the

assessment of the library quality, library sequencing was carried out on HiSeq 2500 system (Illumina) using single-ended 50-bp reads. The reads were mapped to the human or mouse genomes and normalized to fragments using the TopHat and Cufflinks software pipeline.

TCR specificity prediction

The specificity of TCR was predicted using the TCRmatch tool of IEDB website (http://tools.iedb.org/tcrmatch/).[20] In brief, CDR3b sequences were uploaded. The filtering threshold was set as 0.9. For each CDR3b, the predicted antigen with the highest score was chosen as the targeted antigen.

Tube formation assay

The tube formation assay was performed as previously described.[54] Briefly, Plate (24 well) was coated with 10 mg/mL growth factor reduced Matrigel (125 μL/well, Corning, Cat# 354263) under chilling condition and incubated for solidification at 37°C for 30 min. Fifty thousand human brain microvascular endothelial cells (HBMECs) (ATCC, Cat# CRL-3245) were mixed with glioma-educated human CD4 T cells at 1:1 ratio with or without 5 μg/mL anti-IL8 antibody (R&D, Cat# MAB208) and seeded on Matrigel-coated wells. Alternatively, medium containing 10 ng/mL IL-8 was used for tube formation. Eight hours later, the wells were captured at multiple fields per well by an inverted microscope. Vessel density was quantified by AngioTool 0.6a.

QUANTIFICATION AND STATISTICAL ANALYSIS

Analysis summary

Statistical analysis and all software used is detailed in the below sub-sections. Statistical details for experiments, including the statistical test used, the value of n, and what n represents, can be found in the figure legends. All p values below 0.05 were considered significant (*$p < 0.05$; **$p < 0.01$; ***$p < 0.001$; ****$p < 0.0001$).

scRNA-seq data analysis

Alignment, filtering, barcode counting and unique molecular identifier counting were performed by using Cell Ranger v.2.1.0. Data were further analyzed using Seurat v.2. Briefly, cells with a percentage of mitochondrial genes below 0.05% were included. Cells with the highest (top 0.2%) or lowest (bottom 0.2%) numbers of detected genes were considered as outliers and excluded from the downstream analysis. Raw unique molecular identifier counts were normalized to unique molecular identifier count per million total counts and log-transformed. Variable genes were selected based on average expression and dispersion. t-SNE or U-MAP plots were generated based on selected principal component analysis dimensions. Marker genes were identified by the Seurat function FindAllMarkers. Scaled expression data of these marker genes were used for creating the heatmaps. Trajectory analysis for T cell fate decision was performed with Monocle v.2. as previously described.[55,56]

For single cell V(D)J datasets, contig assembly and paired clonotype calling was performed by Cell Ranger vdj pipeline. If cell barcode contained multiple α/β chains, the first assembled contig was used to identify CDR3 (Complementarity Determining Region 3) amino acid sequences. T cells with paired productive TCR α and β chains were retained. Clonotype was defined by unique combination of CDR amino acid sequences of α and β chains.

Mass cytometry data analysis

Mass cytometry data were analyzed using cytobank (https://premium.cytobank.org).[47] Data analysis was performed using viSNE algorithms on gated live single cells. Cell populations were defined based on marker expression distribution in the figure according to standard definitions of cell types: T cells, $CD3^+$; B cells, $CD19^+$; NK cells, $CD56^+$, $CD3^-$, $CX3CR1^-$; CD4 T cells, $CD3^+$ $CD4^+$; $CD8^+$ T cells, $CD3^+$ $CD8^+$; and $\gamma\delta$ T cells, $CD3^+$ $TCR\gamma\delta^+$.

Single-nucleus RNA sequencing (snRNA-seq) data analysis

The snRNA-seq raw data of the glioma tumor microenvironment were downloaded from https://portal.gdc.cancer.gov/projects/CPTAC-3.[33] Data preprocessing was performed as previously described. Briefly, alignment, filtering, barcode counting, and unique molecular identifier counting were performed by Cell Ranger v.3.0.1. Seurat v3.1.2 was used for all subsequent analyses. A series of quality filters were applied to the data to remove those cell barcodes that fell into any one of these categories recommended by Seurat: too few total transcript counts (<300); possible debris with too few genes expressed (<200) and too few UMIs (<1,000); possibly more than one cell with too many genes expressed (>10,000) and too many UMIs (>10,000); and possible dead cells or a sign of cellular stress and apoptosis with too high of a proportion of mitochondrial gene expression over the total transcript counts (>10%). Each sample was scaled and normalized using Seurat's 'SCTransform' function to correct for batch effects (with parameters: vars.to.regress = c("nCount_RNA", "percent.mito"), variable.features, n = 3000).

T cell distribution analysis with spatial Ivy Glioblastoma Atlas Project (GAP) data

The Ivy GAP RNA-seq data and sample annotation containing anatomic location were downloaded from the Ivy GAP website (https://glioblastoma.alleninstitute.org/static/download.html).[57] The T cell marker genes were picked, and their expression levels were normalized to the average and divided by the standard deviation. The final value was used to generate heatmap.

Signature score calculation for T cells clusters

We calculated each cell type score as previously described.[58–60] Briefly, we firstly identified differentially expressed genes (DEGs) between CD4_*IL8* cluster and other clusters with moderated t test implemented by the R package limma.[61] Stringent thresholds (fold change $\geq$4 and p value <0.01 adjusted by the Benjamini–Hochberg method) were then applied to define signature genes for CD4_*IL8* cluster. As a result, we identified 32 signature genes for IL-8-producing $CD4^+$ T cells, and calculated the score by averaging the z-score-transformed expression of these 32 genes (Table S5). This method was accordingly applied to calculate signature scores for other T cell clusters.

Gene set enrichment analysis (GSEA)

GSEA[62,63] was used to assess whether myeloid cell-related genes were enriched in the CD4_*IL8* T cell subset. To this end, we filtered 367 highly expressed myeloid cell genes in the GSE166418 dataset with the criteria of a fold change >2 and $p < 0.01$. Then, we analyzed the enrichment of these myeloid cell highly expressed genes in CD4_*IL8* vs. CD4_Naive. The GSEA permutation was set as 1,000 times. Adjusted $p < 0.05$, false-discovery rate (FDR) < 0.25, and normalized enrichment score (|NES|) > 1 were considered significant enrichment.

Statistics

Comparisons between two different groups were performed with unpaired or paired two-tailed Student's t tests. Survival analysis was performed by the Kaplan–Meier method, with the log rank test for comparison. HRs and their 95% CIs were calculated using stratified Cox proportional hazards regression models. The correlation p values were calculated using stratified two-tailed test as indicated in figure legends. The cutoff point optimization of patients in the TCGA database was calculated by SPSS statistics software. Statistical analysis was performed with GraphPad Prism 9. All quantitative data are presented as the mean ± SD or mean ±95% CI as indicated in figure legends.